

Article

Simulated Radio and Neutrino Imaging of a Microquasar

Theodoros Smponias ¹

¹ Directorate of Primary Education of the Ionian Islands, Corfu, Greece
* Correspondence: t.smponias@hushmail.com

Abstract: Microquasar stellar systems emit electromagnetic radiation and high-energy particles. Thanks to their location within our own Galaxy, they can be observed in quite detail. Still, many of their inner workings remain elusive, hence the usefulness of a simulation as the link between observation and theory. In this paper, both high-energy particle emission and synchrotron radio emission, from simulated microquasar jets, are calculated using special relativistic imaging. A finite ray speed imaging algorithm is employed, acting on hydrocode data, producing synthetic images, as seen from a stationary observer. A hydrodynamical model is integrated with the above emission models. Synthetic spectra and maps are then produced, that may be compared to observations by detector arrays. As an application, the model synthetically observes microquasars during an episodic ejection, at two different spatio-temporal scales, one at the neutrino emission region scale and the other at the synchrotron radio emission scale. Results are compared to the sensitivity of existing detectors.

Keywords: ISM: jets and outflows; stars: winds–outflows; stars: flare; radiation mechanisms: general; methods: numerical

1. Introduction

Microquasars (MQs) include a binary stellar system, with a main sequence star orbiting a collapsed stellar remnant. [1]. Material from the star accretes onto the compact object, resulting in the production of a pair of relativistic ejections, moving in opposite directions, largely perpendicular to the orbital plane of the binary. Those ejecta form into jets, which emit from radio to very high energy (VHE) γ rays and neutrinos [2], [3], [4], [5], [6], [7], [8], [9], [10], [11], [12], [13].

As shown in [2], apparent superluminal motion in MQs suggests that jets comprise bulk hadron flows. The assumption of equipartition [6] leads to high magnetic field estimates, especially for the inner jet [14]. The latter, together with the fluid approximation for the jet matter due to the presence of tangled magnetic fields [15] [16], lay the foundation for jet magnetohydrodynamic (MHD) approximation. A toroidal magnetic field may contribute to jet collimation along its path [14] [17], while confinement from surrounding winds is also a possibility [18] [6].

A turbulent fluid jet region can give rise to a variety of signals, from radio to γ rays. Furthermore, cascades of high-energy particles in the jets produce different particle populations linked by the transport phenomenon. The emergence of neutrinos that leave the system could be detected by modern arrays.

In this work, the production of radio synchrotron emission and of very high energy (VHE) neutrinos from generic MQ jets are studied, using the method of dynamic and radiative relativistic MHD simulation, where model physical space is divided into computational cells. The effects of a wind from the companion star are also included.

Adopting the one-zone (homogeneous) emission model at each eligible hydrocode cell, the solution of successive transport equations, connecting particle distributions in a cascade, provides the intensity of emitted neutrinos, as a function of local dynamic and radiative jet parameters. Particle cascade calculations, acting on hydrocode data

Citation: Smponias, T Imaging of a microquasar. *Journal Not Specified* 2021, 1, 0. <https://doi.org/>

Received:

Accepted:

Published:

Publisher's Note: MDPI stays neutral with regard to jurisdictional claims in published maps and institutional affiliations.

Copyright: © 2023 by the authors. Submitted to *Journal Not Specified* for possible open access publication under the terms and conditions of the Creative Commons Attribution (CC BY) license (<https://creativecommons.org/licenses/by/4.0/>).

41 output, employ results from Monte Carlo simulations [19,20]. This way, a cell's physical
42 parameters are directly connected to its particle emission. Cascade timescale is taken as
43 much smaller than the dynamic timescale of the modelled system. Repeating the above
44 calculations over a number of different energies, provides a neutrino energy spectrum
45 at each jet point. Line-of-sight integration follows, leading to production of synthetic
46 neutrino images and spectra of the model system.

47 Charge neutrality is assumed in the jets, coupling the bulk flow proton and electron
48 distributions dynamically, through a relativistic MHD simulation. The latter provides,
49 at each cell, the bulk proton density and also the magnetic field. High energy hadron
50 and lepton populations, obtained through shock front acceleration in the jets, using the
51 one-zone model at each computational cell, lead to synchrotron emission [6], taking
52 into account local magnetic fields. Here we focus on the radio synchrotron band, where
53 the spectrum is flat or inverted and the emission from protons is essentially negligible
54 (see figure 5 of [6]). As shown in the Appendix (Section 7.1), the inner jet region of \simeq
55 10 mas is modelled here, where a flat radio spectrum typically occurs. Comparable
56 lepton and hadron contributions to radio synchrotron only occur when much more
57 energy is assigned to hadrons than to leptons. As an approximation, only synchrotron
58 emission from accelerated jet electrons is modelled here, using the formalism of [21].
59 Self-absorption is also included. Electron pressure is considered low enough to facilitate
60 the above configuration.

61 Consequently, local MHD jet properties, as provided by the MHD model, allow
62 the calculation of local radio synchrotron emission and absorption coefficients. Down
63 the pipeline, this may lead to synthetic radio maps of the model system. Combined,
64 the study of synchrotron and neutrino emission from the jets may offer an improved
65 understanding of high energy processes in the system.

66 In the current work, the finite nature of the speed of light is now taken into account
67 when viewing the model jet, which constitutes an improvement over previous work
68 [22]. Imaging a relativistically-moving macroscopical object, opens a window to a rather
69 unexpected and even strange world of peculiarities. The basic mandates of Special
70 Relativity, regarding length contraction and time dilation, constitute a mere beginning,
71 in the quest for comprehension of the actual appearance of a fast-moving object [23–27].
72 An observer shall see the object view affected by a number of relativistic distortions
73 [28–30].

74 The transformation of electromagnetic emissions, from the jet frame of reference
75 to the Earth frame, requires performing the Lorentz/Poincaré transform [18,28,31,32].
76 Applying the latter transform for imaging purposes, aims to reconstruct what the ob-
77 server will actually see. Relevant to this point, [33] argues about the important difference
78 between vision and measurement in Special Relativity, presenting that difference in a
79 geometrical manner.

80 Radiation emitted from a jet is therefore subject to relativistic effects [18,34], in-
81 cluding time dilation, relativistic aberration and frequency shift, leading collectively
82 to what is known as Doppler boosting and beaming [28,32,35]. Aberration causes the
83 fast-moving object to actually appear rotated to a stationary observer [24,25,28,36], a
84 phenomenon sometimes called the Terrell-Penrose rotation.

85 Ray-tracing methods provide excellent quality of relativistic images, despite lacking
86 in terms of efficiency, compared to such techniques as polygon rendering [30]. In this
87 work, a relativistic imaging method is employed, whereby time-resolved hydrocode
88 data are being crossed by rays, called lines of sight (LOS), either focused or parallel to
89 each other. Synchrotron emission is subject to Doppler boosting effects, depending on
90 local velocity orientation.

91 Furthermore, the aforementioned high-energy proton distribution is Lorentz-transformed
92 to a stationary frame, exhibiting dependence on speed and orientation, favouring particle
93 emissions along the direction of local velocity [37]. The resulting expression demonstrates
94 relativistic boosting properties, in a manner broadly comparable to the Doppler boosting

of E/M radiation. A cascade of particle distributions then emerges, affected by local MHD properties, eventually leading to neutrino emission, which then escape the system. Subsequently, with neutrinos, imaging ‘rays’ move at the finite speed of light.

Simulating the above processes may help clarify inner workings of the jets and their environs, leading to a more accurate description of the system of interest.

In the remaining of this paper, theoretical background is laid, for both radio synchrotron and neutrino particle emission (Section 2). Section 3 briefly describes the employed software pipeline. The model setup is presented next (Section 4), including various model parameters. In Section 5 the results are presented and discussed. Finally, in Section 6 useful conclusions are drawn from the current work and possible future applications are proposed.

2. Theoretical Background

2.1. Radio synchrotron emission and self-absorption

Adopting high energy electron and proton acceleration at shock fronts [21], a power-law high energy distribution is assumed for each of the aforementioned particle species. Electrons are discussed in this subsection, protons in the following one. For electrons,

$$N_{(E)} = N_0 E^{-\gamma_c} = K_{pl} \rho_{4d} E^{-\gamma_c} \quad (1)$$

where K_{pl} is a power law constant for high energy jet electrons. Through K_{pl} , the reference electron density N_0 is taken proportional to local bulk flow proton density ρ_{4d} , based on charge neutrality. Bulk flow proton density ρ_{4d} , assumed proportional to electron reference density everywhere, is provided for spatiotemporal points by MHD code. Thus a link is established between hydrocode quantities and electron populations in the jet.

For accelerated protons and electrons, a high energy cutoff is adopted, according to the Hillas criterion, [38]. $E_{max} = ZqBR_s$ for the maximum energy E_{max} achieved through acceleration, for a particle of charge q , and atomic number Z , within a magnetic field B , in an accelerator of size R_s . For a size of a computational cell, of our radio-scale model, of 10^{13} cm, and a magnetic field of order of 10 G, the above equation shall give a result into the TeV scale, well above the radio band, which is of interest in this subsection. Furthermore, the energy cutoff from dominant cooling mechanisms, for radio-band synchrotron from a microquasar, lies above radio-band energies [6]. Consequently, for the rest of the radio calculation, the high energy cutoff may be implied, since the focus is on lower electron energies, included in radio emission.

On the other hand, for high energy protons, a cutoff of $E_{max}=10^6$ GeV is employed, see Section 10 in the Appendix.

Synchrotron emission and absorption coefficients are then calculated, following [21]

$$\epsilon_\nu = f_{pp(4d)} K_{pl} c_5(\gamma_c) \rho_{4d} (\overrightarrow{B_{4d}} \sin(\widehat{\text{LOS}, \overrightarrow{B_{4d}}}))^{\frac{(\gamma_c+1)}{2}} \left(\frac{f_{obs}}{2D_{4D_{local}} c_1} \right)^{\frac{(1-\gamma_c)}{2}} D_{4D_{local}}^2 \quad (2)$$

$$k_\nu = f_{pp(4d)} K_{pl} c_6(\gamma_c) \rho_{4d} (\overrightarrow{B_{4d}} \sin(\widehat{\text{LOS}, \overrightarrow{B_{4d}}}))^{\frac{(\gamma_c+2)}{2}} \left(\frac{f_{obs}}{2D_{4D_{local}} c_1} \right)^{\frac{(-4-\gamma_c)}{2}} D_{4D_{local}}^2 \quad (3)$$

$f_{pp(4d)}$ is a proton profile function, f_{obs} is the observing frequency, $\frac{f_{obs}}{D_{4D_{local}}}$ is the calculation frequency (blue-shifted or red-shifted according to the relative orientation between local LOS and local velocity). $\overrightarrow{B_{4d}}$ is the local magnetic field vector, $\widehat{\text{LOS}}$ is the line of sight (LOS) vector, at an angle $(\widehat{\text{LOS}, \overrightarrow{B_{4d}}})$ to the magnetic field spatial vector. $D_{4D_{local}}$ is the local Doppler factor of jet matter at a computational cell, calculated as $D = \frac{\sqrt{1-u^2}}{(1-u*\cos(\text{losu}))}$, $\text{losu} = (\widehat{\text{LOS}}, \overrightarrow{u})$ being the angle between the LOS and the local velocity u , $0 \leq u \leq 1$.

(Section 9.3.3). γ_c is the electron power law index, taken as 2 in the current work, equal, for simplicity, to the proton power law index. Quantities c_i , $i=[1,6]$, are $c_1=6.27\times 10^{18}$, $c_2=2.37\times 10^{-3}$, $c_3=1.87\times 10^{-23}$, $c_4=4.2\times 10^7$

$$c_5 = 0.25c_3\Gamma\left(\frac{3\gamma_c - 1}{12}\right)\Gamma\left(\frac{3\gamma_c + 7}{12}\right)\left(\frac{\gamma_c + \frac{7}{3}}{\gamma_c + 1}\right) \quad (4)$$

$$c_6 = \frac{1}{32}\left(\frac{3\times 10^{10}}{c_1}\right)^2 c_3\left(\gamma_c + \frac{10}{3}\right)\Gamma\left(\frac{3\gamma_c + 2}{12}\right)\Gamma\left(\frac{3\gamma_c + 10}{12}\right) \quad (5)$$

where Γ is the Gamma function.

The above coefficients are computed at each point (computational cell) of the model jet system. The angle ($\widehat{\text{LOS}}, \widehat{B_{4d}}$) between the LOS and the local magnetic field B , is calculated at each jet point, Section 9.3.4.

In the above, only two Doppler factors and a frequency shift factor are included. The reason is to allow detection of the receding blob in the synthetic radio images. Additional Doppler factors can be employed, see Section 9.3.

2.2. Nonthermal proton density

Neutrino emission from model jets comes from proton–proton interaction between a distribution of high-energy (non-thermal) protons and bulk flow protons [2,5,6,9,19,20, 22]. Some thermal protons gain energy at shock fronts within the jet, according to the first-order Fermi acceleration mechanism, within a time frame of [39], [15], [16]

$$t_{\text{acc}}^{-1} \simeq \eta \frac{ceB}{E_p}, \quad (6)$$

where B is the magnetic field, E_p the non-thermal proton energy, e the particle charge, and c the speed of light. η is an acceleration efficiency parameter, for the process of efficient particle acceleration in moderately relativistic shocks, near the base of the jet [39]. In general, η depends on shock velocity and on the local diffusion coefficient [40]. As an approximation, $\eta = 0.1$ [39].

A power-law energy E distribution is employed for non-thermal protons $N_p = KN_{p(0)}E^{-\alpha}$ [18], where K is a constant much smaller than unity, N_p is the hot proton number density and $N_{p(0)}$ the cold proton number density, with either $\alpha \approx 2$ [5], or a variable α [9], where α is the proton spectral index in the local jet matter frame. A transport equation may also be used in order to find the distribution [5].

The high-energy proton distribution is considered isotropic in the jet frame, assuming that, at each jet point, $l_{\text{sc}} < l_r$, where l_{sc} is the scattering length and l_r the radiative length. The above approximation is based on the need to preserve, after every bounce, at least some proton energy [16]. Scattering length l_{sc} is less than radiative length l_r , otherwise, the proton would not have any energy left after the bounce, negating the acceleration process.

A hypothetical anisotropy of hot proton distribution can be reflected to neutrino distribution [41], potentially introducing anisotropy in the jet frame's particle emission field.

2.3. Neutrino emissivity

For each computational cell, a high energy proton distribution is transformed (Appendix: Section 10) [37] from cell's frame to our frame, using the angle of local velocity to the LOS crossing that cell. Thereafter, a local particle cascade emerges at that cell. From protons to pions and then to prompt neutrinos (an alternative route, not modelled here, is: from protons to pions, muons and then delayed neutrinos), successive particle populations are linked by transport equations. At each cell, as shown in the Appendix, Section 10, the transport equation is resolved in succession twice, from a

¹⁶⁶ power-law high energy proton distribution to pions and then to neutrinos, resulting in
¹⁶⁷ the production of prompt neutrinos [5,6,19,20].

$$Q_{\pi \rightarrow \nu}(E) = \int_E^{E_{\max}} dE_{\pi} t_{\pi}^{-1}(E_{\pi}) N_{\pi}(E_{\pi}) \frac{\Theta(1 - r_{\pi} - x)}{E_{\pi}(1 - r_{\pi})}, \quad (7)$$

¹⁶⁸ E is neutrino energy, E_{π} is pion energy, N_{π} is pion number density (Section 10), $x =$
¹⁶⁹ E/E_{π} , $r_{\pi} = (m_{\mu}/m_{\pi})^2$ (m_{μ} , m_{π} are muon and pion mass respectively) and t_{π} is the pion
¹⁷⁰ decay timescale. $\Theta(\chi)$ is the theta function [6,42]. $E_{\max} = 10^6$ GeV. The calculation
¹⁷¹ leading to the above result can be found in the Appendix, Section 10. Neutrino emission
¹⁷² is calculated for each eligible hydrocode cell. Imaging process may incorporate either
¹⁷³ parallel LOS's or a focused beam, where each LOS follows a slightly different path to a
¹⁷⁴ common focal point [43]. A synthetic image of the model system is thus produced.

¹⁷⁵ 3. Computer programs used

¹⁷⁶ 3.1. rlos

¹⁷⁷ rlos [43] is an evolution of classical imaging code used in earlier works [44–46]. A
¹⁷⁸ ray, or LOS, emanates from each pixel of the imaging side of the Cartesian 3D compu-
¹⁷⁹ tational domain, Figure 1, or from a focal point, aiming at a point on a fiducial screen,
¹⁸⁰ Figure 17 (Appendix). Either way, there is an imaging plane. Along the LOS, the equa-
¹⁸¹ tion of radiative transfer is solved at each cell, using local emission and absorption
¹⁸² coefficients. Depending on the situation modelled, coefficients may either be directly
¹⁸³ calculated, or outsourced to another program.

¹⁸⁴ rlos is organized in two outer spatial loops, running over the imaging plane and
¹⁸⁵ an inner 1-dimensional spatial loop, advancing in pairs of steps, one for each direction
¹⁸⁶ angle (azimuth and elevation), running over the length of a LOS (Figure 16). At the
¹⁸⁷ innermost lies a conditional temporal loop, running over the hydro data time span (see
¹⁸⁸ also Appendix, Section 9.6.1). Since the emission coefficients' calculation load is global,
¹⁸⁹ it is performed, where feasible, before the loops, in array-oriented operations, in order to
¹⁹⁰ improve performance.

¹⁹¹ Lines of sight are drawn starting from a focal point (focused beam), or from a
¹⁹² pixel of the yz or xz side (parallel rays) of the domain, (Figure 1, and, in the Appendix,
¹⁹³ Figures 12 and 17). Tracing their way along the given direction, they reach a length of
¹⁹⁴ $\sqrt{(x_{\max}^2 + y_{\max}^2 + z_{\max}^2)}$, where $x_{\max}, y_{\max}, z_{\max}$ are the dimensions in cells of the com-
¹⁹⁵ putational domain. In practice, on reaching the ends of the domain, an LOS calculation
¹⁹⁶ halts, and some LOSs may thereby end up being shorter than others. The above process
¹⁹⁷ is repeated within a 2D loop running over the imaging plane, with each LOS correspond-
¹⁹⁸ ing to a single pixel of the final synthetic image. As an approximation, along an LOS, no
¹⁹⁹ sideways scattering is considered.

²⁰⁰ A model astrophysical system geometry may be directly inserted into rlos. As an
²⁰¹ example, a 'conical' jet setup [47], is available to the user. Alternatively, data output from
²⁰² a hydrocode may be employed, as in the current paper, using PLUTO [48].

²⁰³ 3.2. The PLUTO hydrocode

²⁰⁴ PLUTO [48] is an open-source, 2D/3D modular hydrocode, a finite-volume/-
²⁰⁵ difference shock-capturing program, meant to integrate a set of (time-dependent) con-
²⁰⁶ servation laws. Initial and boundary conditions are conveniently assigned through an
²⁰⁷ equivalent set of primitive variables. The relevant systems of equations may include
²⁰⁸ hydrodynamics (HD), magnetohydrodynamics (MHD), and their special-relativistic
²⁰⁹ counterparts, RHD and RMHD, respectively, in either two or three spatial dimensions.
²¹⁰ The solution of conservation laws is produced through discretization on a structured
²¹¹ mesh, a logically rectangular grid surrounded by a boundary with additional ghost cells
²¹² in order to implement boundary conditions. The grid may either be static or adaptive,

and various coordinate systems are available. The programme may run efficiently in parallel on various platforms.

3.3. nemiss

nemiss [49] [22] calculates neutrino emission and spectra from the output of PLUTO hydrocode. It stands between PLUTO and rlos, taking the burden of global particle cascade calculations off the shoulders of rlos, helping form the pipeline PLUTO-nemiss-rlos. Synthetic neutrino images are produced, taking into account the finite speed of emitted neutrinos. Doppler boosting and frequency shift are switched off in rlos, when imaging with neutrinos.

3.4. Software information

Intensity plots of the pair of jets are created using Veusz, a software for plotting data written by Jeremy Sanders and contributors, and distributed under the GNU/GPL licence. rlos and nemiss [49], written by the author, are available under the LGPL licence. PLUTO was written by Andrea Mignone and collaborators, and is available under GNU/GPL.

4. Model setup

The MQ system is represented at two different scales, one for modelling neutrino emission and another for radio emission. At the smaller scale, meant for neutrinos, an accretion disk is assumed around the collapsed object [50], while the companion star itself lies outside the model space. A continuous ejection, representing the beginning of a new blob, is employed.

On the other hand, at the radio emission scale, both participants of the binary system lie within the same computational cell, while a sequence of plasmoids is now employed.

In both cases, twin jets emerge from near the compacted star, with a collimating toroidal magnetic field component. The field is set higher at the neutrino emission scale.

4.1. Radio synchrotron emission model

A twin model jet system is synthetically observed, using radio synchrotron emission at a frequency of 8 GHz. A 3D homogeneous Cartesian coordinate system is employed. Jets enter the grid at a speed of $0.8c$, emanating from a central location in the grid.

The jet is synthetically observed using synchrotron emission and self-absorption [21]. At each computational cell, the angle between the local magnetic field and the LOS is calculated, leading to the cell's emission and absorption coefficients. Likewise, the local angle between LOS and velocity, facilitates each cell's Doppler boosting calculation.

A sequence of twin relativistic blobs is ejected from the jet base, moving in opposite directions, at an angle to the observer. One jet is approaching, the other is receding. The model jet is made of a series of such plasmoids, ejected for 30 hydrocode time units every 100 time units. Two separate hydrocode runs were performed, one with a heavier jet and another with a lighter jet.

The heavier radio jet in the model is very strong, at about $10^{43} \text{ ergs}^{-1}$, whereas the lighter one stands at around $10^{41} \text{ ergs}^{-1}$. These values are generally on the higher end for a MQ jet, especially the heavier one. This in part can be attributed to the low resolution employed, which defines a minimum nozzle diameter, while opting to keep realistic jet densities. The lighter radio jet model is generally closer to an actual MQ, while the heavier model run is mainly included for the purpose of comparison. The details of the runs are shown in Table 1.

A toroidal magnetic field of 10 G is introduced, resulting to a magnetic energy density below the kinetic energy density (see Appendix, Section 8). For simplicity, the magnetic field in this run was initiated wrapped around the y-axis.

At regular time intervals, a model system instance is saved to disk. Then, synchrotron emission ϵ_ν and absorption κ_ν coefficients are calculated at each spatial point, for a given set of angles of observation within rlos. A series of four-dimensional arrays are thus obtained, through which lines-of-sight travel. Rays start at the moment of observation and move backwards, in both space and time, in order to meet blobs at an earlier instant.

The angle to y axis is 55 degrees and the finite-ray speed, focused beam, imaging method is employed, in all radio imaging runs. As a test, an RMHD run was also performed with an angle to the LOS of 55 degrees, in order to better visualize apparent superluminal motion. A simplified stellar wind construct is employed, its density inversely proportional to the distance from the companion star [44].

273 4.2. Neutrino emission

At the neutrino-scale model scenario, twin hadronic jets are simulated with PLUTO code [22]. Jets are viewed from the side, while the finite-ray speed imaging mode of rlos is now employed.

For the given model view orientation, neutrino emission is calculated at each eligible spacetime point of the computational grid, using nemiss [49]. Emissivity of neutrinos is separately calculated, at individual computational cells, using the angle (los,u) formed between LOS and local velocity. Parameters of this scenario appear in Table 1. The binary companion now resides outside the computational grid, at the position (400, 0, 400), affecting the model with its stellar wind [22]. The accretion disk is simulated approximately as a disk structure, and a basic accretion disk wind construct is also included.

The jet being continuous is a feature compatible with the radio scale model, since at the ν -scale, the time unit of the model is 1000 times less than in the radio-scale. The beginning of the injection process of a single radio plasmoid is conceptually modelled at the neutrino-scale scenario.

Furthermore, rlos [43], is employed, which reads the combined results of PLUTO and nemiss, producing synthetic neutrino images of the model system using the focused beam geometry setup.

At the ν -scale, the relativistic transformation of the hot proton distribution by [37] is employed. The magnetic field is toroidal and adjusted for equipartition, $B_{\vec{r}z} = \sqrt{8\pi\rho_{\vec{r}z}}$, [15] [16], (Appendix: Section 8). External magnetic fields can be taken to be smaller [51]; therefore, as a first-order approximation, they are omitted from the model's surrounding winds.

Neutrino emission, at each computational cell, is calculated using the formalism presented earlier in this paper (Section 2.3), and in the Appendix (Section 10). This method, albeit costly, allows for obtaining a separate neutrino emission from each spatiotemporal point of the model. Thus, we aim for result

$$I_\nu = I_\nu(\vec{r}, t) \quad (8)$$

where 3D space location \vec{r} is represented by the x, y, and z coordinates of the computational cell in question. Time t is obtained from the time tag of the hydrocode snapshot where the cell belongs¹. The above equation is globally applied to all selected PLUTO data (the user may select beginning and end times for the global calculation).

For reasons of economy, a double filter is applied, whereby neutrino emission is calculated only at cells whose velocity aims not too far from the LOS ($\cos(\text{losu})$ greater than 0.08), and their speed is at least 0.1c.

At the neutrino scale, the jets' kinetic power was set to $L_k=2 \times 10^{38}$ (see the appendix). [6] argue a 10% Eddington jet kinetic luminosity, leading to $L_k=10^{38} \text{ ergs}^{-1}$ for

¹ MHD datasets are 4-dimensional, including the dimension of time

³⁰⁶ a $10 M_{\odot}$ black hole, which is comparable to the current case. [6] adopt either $\frac{L_p}{L_e} \simeq 100$
³⁰⁷ or $\simeq 1$; we select the former case, which means a hadronic jet. As an approximation,
³⁰⁸ neutrino emission from a high-energy proton distribution is obtained, omitting contribu-
³⁰⁹ tions from the corresponding high-energy electron distribution. The jet base is situated
³¹⁰ near the centre of a Cartesian grid.

³¹¹ 4.3. Model parameters

³¹² Table 1 shows a number of simulation parameters. Those include computational cell
³¹³ length, jet density, and winds' maximal densities (those gradually declined away from
³¹⁴ their sources)^{2 3}. In PLUTO, the piecewise linear method was set up using the MUSCL
³¹⁵ Hancock integrator, with an ideal equation of state. In the neutrino-scale simulation,
³¹⁶ the binary companion is located outside the grid, and was estimated to be at most up to
³¹⁷ an order of magnitude more massive than the compact object. Jet speed is 0.8c.

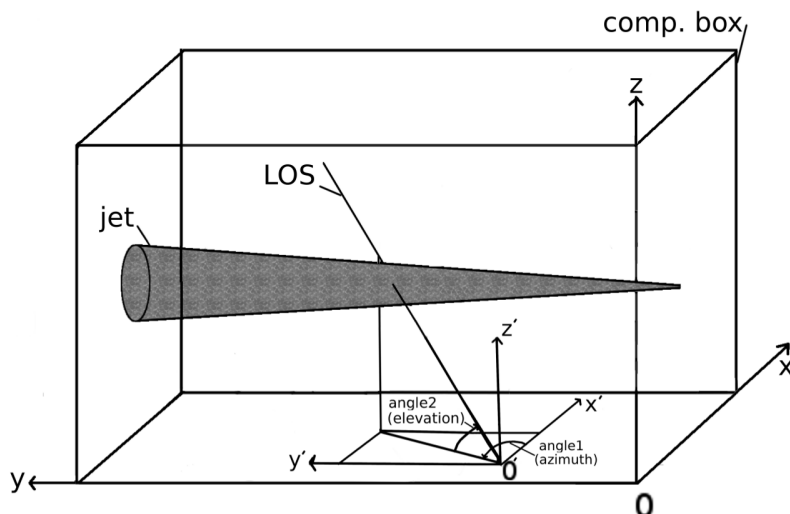


Figure 1. 3D schematic view of rlos applied to a model astrophysical jet, for the parallel rays' setup. Imaging side of the computational box is the yz plane located on the side of the box apparently closer to the reader. Lying on the yz plane, O' is the point of origin of a random LOS with its own dashed coordinate system $x'y'z'$. Alternatively, the imaging plane may also lie on the xz side of the box.

³¹⁸ 5. Results and discussion

³¹⁹ Twin jet simulations of this paper represent three fiducial microquasars, dynamically
³²⁰ set up to resemble a number of actual microquasars. In the synthetic imaging process
³²¹ (rlos code), the focused beam geometry is employed, in combination with a finite ray
³²² speed. Synthetic images are projected on a fiducial imaging screen, parallel to the side of
³²³ the grid (YZ), before the beam converges to a focal point, Figure 17.

³²⁴ In general, the imaging process may or may not use all snapshots available to it
³²⁵ depending on the light crossing time of its model segment (adjusted through the clight
³²⁶ parameter in rlos, Subsection 9.4). Trying to read more snapshots than what is loaded
³²⁷ corrupts the hydrocode time array of rlos, called T, resulting in errors. As mentioned

² At the neutrino scale, jet kinetic luminosity is 2.5×10^{38} erg/s, using a low spatial resolution of $60 \times 100 \times 50$. Due to limited computing resources, such a low resolution was necessary, in order to accommodate both the heavier neutrino emission calculation that followed and the time-resolved nature of the calculations, which essentially leads to four-dimensional datasets.

³ At the radio scale model, the use of temporally resolved data, consuming computing resources, and the use of a fixed homogeneous grid, also necessitates a smaller spatial resolution, namely $60 \times 100 \times 50$, thus a larger computational cell. Radio-scale model jets are then more powerful, in order to keep their densities realistic, at the low resolution employed. At the jet nozzle, this means a thicker jet. Opting to keep jet density realistic, overall kinetic luminosity then becomes higher than normal, mainly in the heavy jet radio model. Nevertheless, a normalization process (electron power law constant K) may, to a certain extent, absorb the effects of artificially increased jet power. On the other hand, synchrotron emission and absorption coefficients do depend, among other things, on local density, so a need arises to focus on density in this context.

above, a double filter was used for velocity and for (los, \mathbf{u}) angle. A minimal velocity and maximal angle were set in order to trigger the calculation of the neutrino emission for a particular cell. This way, the expensive part of the simulation was only performed where it was really worth it. This partly alleviated the discrepancy between computational costs of the dynamic and the radiative parts of the model. A similar filter was applied for (los, \mathbf{B}) angle. The use of filters highlights sideways emission from jet elements with near-relativistic velocities roughly perpendicular to the jet axis.

An important aspect of this modelling approach is that a cell has different visible emissivity from Earth than that of its neighbours. That is because each cell may differ from the next one in terms of both speed and orientation to us. Consequently, the output of a hydrodynamic model shall differ from a steady-state one. Individual flow elements may appear either boosted or de-boosted, depending on their speed's orientation to the observer.

Even from the side, adequate emission may be obtained, due to elements of the flow moving relativistically sideways, especially during the initial expansion of the jet's front. Furthermore, delays in arrival of emission emanating from the inner part of the jet, mean the initial violent interaction between the jet and the surrounding wind, still affects synthetic images taken at subsequent time instants. Inner winds heavier than the jets, as was the case in the model runs, further prolong the effects of siderreal emission on the images, by temporarily containing the jet's 'bubble' near the jet base. Thus, initial jet expansion still echoes at images taken later on in the simulation.

Distances in the synthetic images are in computational cells, where, in this work, 1 cell = 2 hydrocode length units. On the other hand, in the hydrocode data renderings, the scale is in hydrocode length units. For each scenario, the hydrocode length unit is shown in Table 1.

5.1. Radio-scale model results

In the radio-scale model, ejected plasmoids form an intermittent twin jet (Figures 2, 3), inflating a twin cocoon while traversing the companion's stellar wind.

Moving away from the jet base, plasmoids seem to expand while crossing ambient wind, in part thanks to a declining wind density away from the binary system. A relatively low toroidal magnetic field further facilitates plasmoid expansion in the model.

An equatorial concentration of wind, and possibly jet, matter forms dynamically (Figures 2, 3), leading to some emission from that region, as seen in the corresponding synthetic radio images that follow.

We can see apparent acceleration, on the sky plane (fiducial model screen), of the approaching plasmoid (Figures 4, 7), while the receding blob moves slower. The approaching blob is also brighter than the receding one. What is more, taking into consideration the finite nature of the speed of light, leads to earlier dynamics affecting images taken at later times. Synthetic radio images of the model system in general show a delay versus actual hydrocode plots bearing the same time tag (Figures 4, 7 and 7).

Toroidal magnetic field threading the blobs, leads to synchrotron emission in the direction of the observer, even from the receding blob, (only two Doppler factors are employed to allow some visibility of receding plasmoids). The model pair of ejected plasmoids demonstrate a quick rise in intensity and a more gradual decrease over time, Figure 5.

A suitable jet orientation setup has a potential for apparent superluminal motion of the approaching jet, especially as seen in Figure 4, also visible in Figure 7.

As a test, a simulation was also run with an approaching 'rectangular' blob. A frontal synthetic image of the blob, moving straight into the fiducial observer (Figure 6), demonstrates the effects of a finite ray speed, as central rays from the rectangle appear stronger than those from its corners, due to delayed arrival of the latter.

380 5.2. *Neutrino-scale results*

381 The PLUTO hydrocode was run, in order to simulate the jets at the neutrino-
382 emission scale (Figure 8). A number of empty PLUTO user parameters were employed in
383 order to accomodate particle emission results later on. The nemiss programme was then
384 run, which calculates neutrino emissions from hydrocode data, for a specific imaging
385 geometry and setup. This programme is able to read 4D spatiotemporal data output from
386 PLUTO into a 5D array, which also includes particle energy as a fifth dimension. Then,
387 nemiss calculates neutrino emission at each point of the 5D data array. Results are then
388 overwritten into suitably prepared data files, which are essentially files of additional,
389 ‘dummy’, user-defined parameters, of the PLUTO hydrocode. Thus, nemiss processes
390 PLUTO output to include a neutrino emission spectrum at each spatiotemporal data
391 point, in the originally dummy PLUTO data files.

392 PLUTO data processed by nemiss were then ready to be read by relativistic imaging
393 code rlos [43], which produces synthetic neutrino images of the system. Over a string of
394 particle energies, the intensity sum of the whole synthetic image of the jets is calculated,
395 leading to a plot of jet neutrino intensities, Figure 9. Furthermore, the model was run
396 at two different time instants, shot number 45 ($t=90$ s) and shot number 90 ($t=180$ s).
397 Relativistic imaging process was used to produce synthetic images, Figure 10.

398 Figure 8 shows narrow jets, slowly expanding into its surrounding winds. This
399 small half-angle is then rather counterintuitively expected to result in a faster decline of
400 neutrino emission with energy, as discussed in the discussion section of [6]. Jets interact
401 with winds, their cocoon expanding sideways as well as forward, into surrounding wind
402 matter. This is important for sideways neutrino emission (Figure 10), because it shows
403 localized neutrino emission along a direction perpendicular to the jet axis.

404 As mentioned earlier, adequate neutrino emission may occur towards Earth, even
405 from MQ jets not aligned with the LOS to Earth. This leads to a rather increased number
406 of MQ candidates for neutrino detection, especially those with rich dynamic interaction
407 with surrounding winds.

408 The above result positively affects emission from a Galactic MQ distribution [22].
409 Even in MQ whose jets point perpendicularly to the LOS to Earth, some relativistic
410 boosting may still appear in parts of the flow moving towards us, especially early on in
411 the ejection event.

Model	Radio heavy	Radio light	ν -scale	Comments	
$l_{\text{cell}} (\times 10^{10} \text{cm})$	2.0×10^3	2.0×10^3	2.0	PLUTO cell	
$\rho_{\text{jet}} (\text{cm}^{-3})$	1.0×10^{12}	1.0×10^{10}	1.0×10^{11}	Jet matter density	
$\rho_w (\text{cm}^{-3})$	1.0×10^{13}	1.0×10^{11}	1.0×10^{13}	Max wind density	
time unit (s)	1.0×10^3	1.0×10^3	1.0	Model time scale (model s)	
$\rho_{dw} (\text{cm}^{-3})$	-	-	2.0×10^{13}	Max disk wind density	
$t_{\text{run}}^{\max} (\text{s})$	242×10^3	242×10^3	204	Model run time	
Method	P. L.	P. L.	P. L.	Piecewise linear	
Integrator	M. H.	M. H.	M. H.	MUSCL-Hancock	
EOS	Ideal	Ideal	Ideal	Equation of state	
physics	RelMHD	RelMHD	RelMHD	PLUTO setup	
B field (G)	10	10	1.0×10^4	Initial toroidal magnetic field	
BinSep (cm)	subcell	subcell	4.0×10^{12}	Binary separation	
$M_{\text{BH}} / M_{\odot}$	-	5-20	3-10	VE compact star mass	
M_{\star} / M_{\odot}	-	10-30	10-30	Companion mass	
$\beta = v_0/c$	0.8	0.8	0.8	Initial jet speed	
L_k^P	10^{44}	10^{42}	2×10^{38}	Jet kinetic luminosity	
Jet type	int.	int.	cont.	intermittent or continuous	
$L_{k(\text{av})}^P$	$\simeq 10^{43}$	$\simeq 10^{41}$	2×10^{38}	Average Jet kinetic luminosity	
Grid resolution	$60 \times 100 \times 50$	$60 \times 100 \times 50$	$60 \times 100 \times 50$	PLUTO grid size (xyz)	
Imaging method	FB	FB	FB	Focused beam	
Time delay	on	on	on	Normal ray speed	
Imaging plane	YZ	YZ	YZ	Fiducial screen parallel to YZ	
Emission	radio-sync	radio-sync	neutrinos	Synthetic emission type	
Code used	PLUTO-rlos	PLUTO-rlos	PLUTO-nemiss-rlos	pipeline portion employed	

Table 1: Three different imaging runs based on three separate underlying hydrocode runs.

DB: rho.0050.vtk
Cycle: 50 Time:50

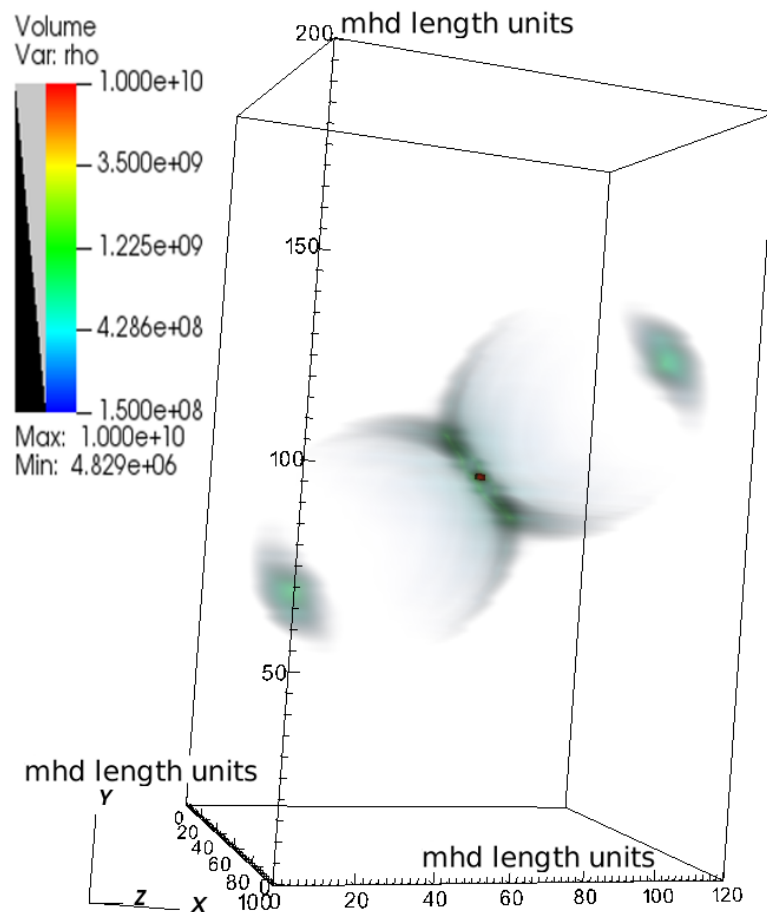


Figure 2. The radio-scale light-jet model, shown at snapshot 50 ($t=100$ ks). The plasmoids traverse the stellar wind moving in opposite directions. Ambient wind is also proportionally lighter than before, therefore resulting to similar dynamics as in the heavier jet model. The plasmoids here also traverse a dense inner stellar wind, giving rise to an equatorial concentration of matter, detectable in the synthetic radio images. Overall, this lighter jet is more realistic in terms of densities and overall kinetic luminosity. In this Figure, length units are from the MHD simulation, where two such units equal a computational cell in length. One MHD length unit here equals 10^{13} cm (Table 1).

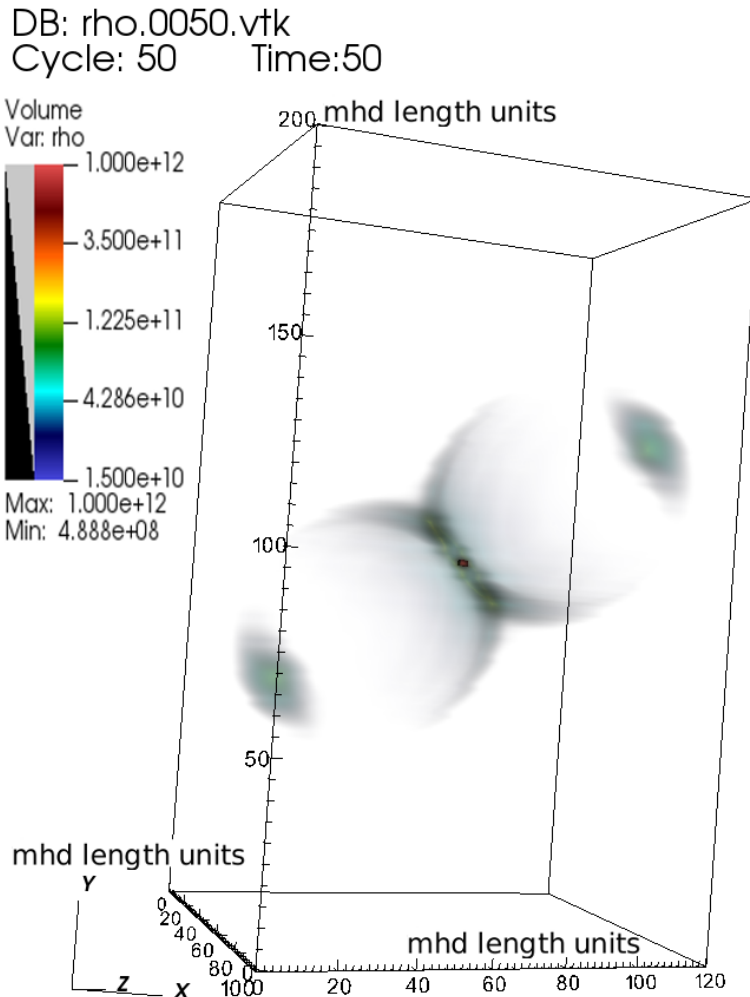


Figure 3. The radio-scale heavy-jet model, shown at snapshot 50 ($t=100$ ks). Blobs traverse the stellar wind moving in opposite directions, forming a pair of intermittent jets. A cocoon formation appears, inflated by fast moving bolides, traversing the ambient wind of the companion star, which is denser than the jet near its base. Inner wind material is being pushed sideways by the jet, facilitating the creation of an equatorial zone, also detected in the synthetic radio images of the model system. In this Figure, MHD simulation length units are employed, where two such units equal a computational cell in length. An MHD length unit here equals 10^{13} cm (Table 1).

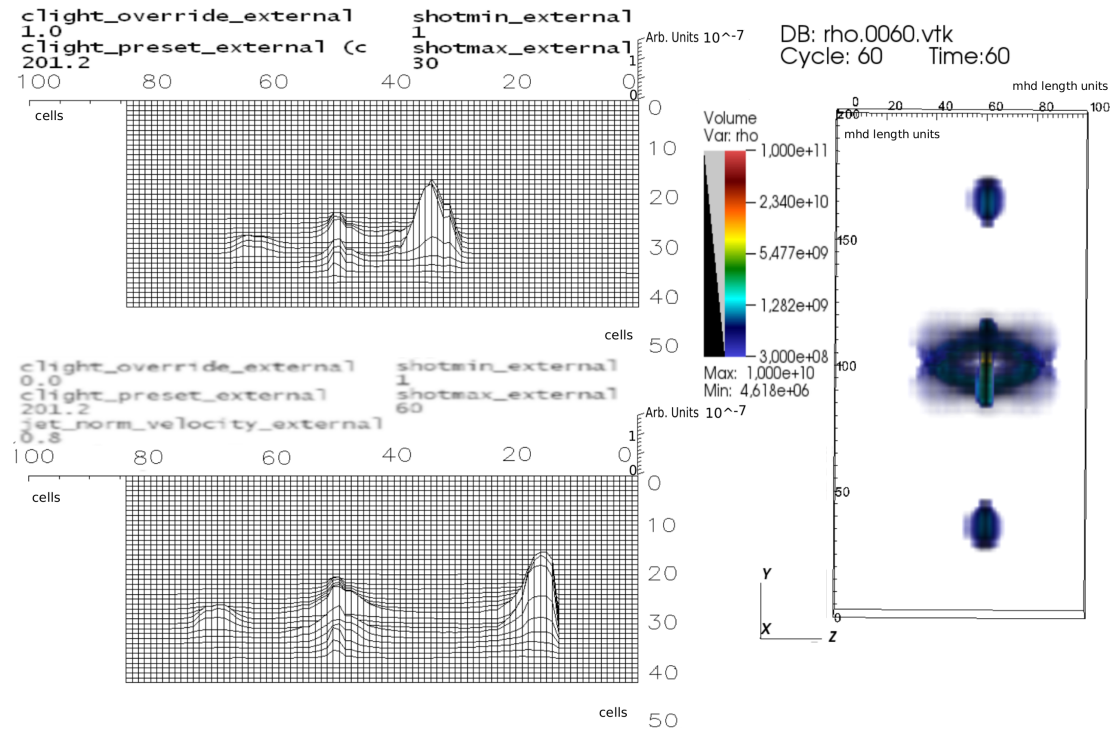


Figure 4. Apparent superluminal motion study setup, the jet at 55 degrees to the LOS, speed at $0.8c$. In the synthetic images (top-left hand corner and bottom left-hand corner), approaching and receding blobs are shown, for a ray speed of $\simeq 200c$ (top left), at shot number 30, and for normal c (bottom left), at shot number 60 (Synthetic images' view is rotated around the z axis by 180 degrees for visual clarity). The difference in timing between the two synthetic images, represents an attempt to match the time-delay of the normal c image to the single-shot image drawn at $200c$. Distances in the synthetic images are in computational cells, where 1 cell equals 2 hydrocode length units. Top left, no real difference exists between approaching and receding plasmoid, resembling the corresponding hydrocode density plot to the right. Bottom left, approaching blob seems on fiducial screen (sky plane) to be much faster than receding blob, a clear demonstration of the apparent acceleration effect. In the right hand side, a hydrocode data rendering of the same model run, the scale is in hydrocode length units. A hydrocode density plot is shown, demonstrating inherently symmetric motion, on a fiducial sky plane, of approaching and receding hydrocode blobs (without using an imaging code).

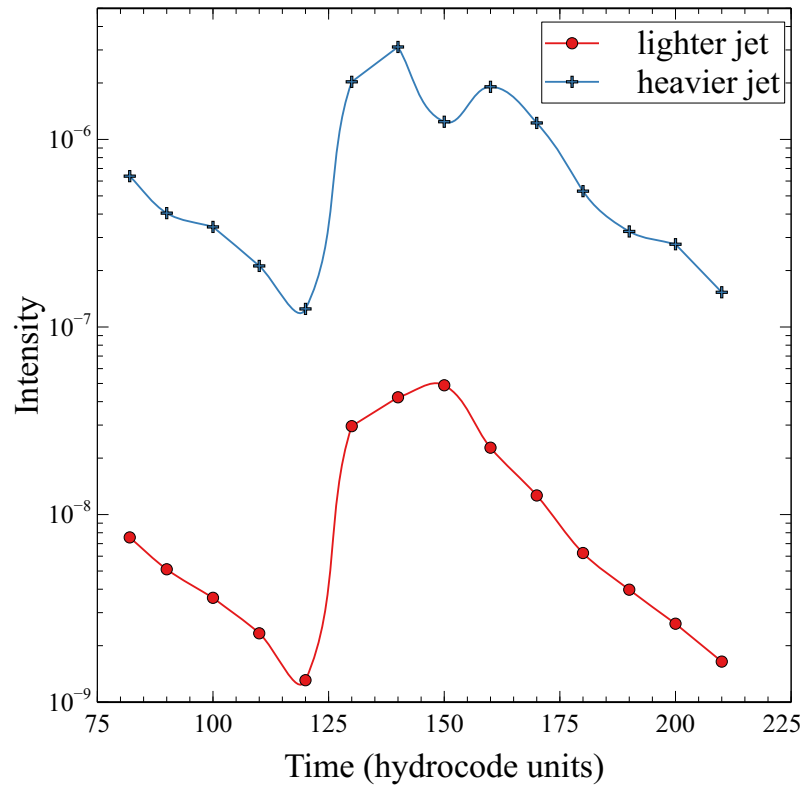


Figure 5. Radio synchrotron model time curves, presenting the evolution of unnormalized intensity over the injection of a new pair of plasmoids. In both cases, a faster rise is followed by a more gradual decline. For the heavy jet case (top curve), previous blobs happen to leave the computational grid at the time of new blob pair insertion, so a drop occurs there. Nozzle densities: Heavy jet, $\rho_{\text{jet}}=10^{12} \text{ cm}^{-3}$, light jet, $\rho_{\text{jet}}=10^{10} \text{ cm}^{-3}$.

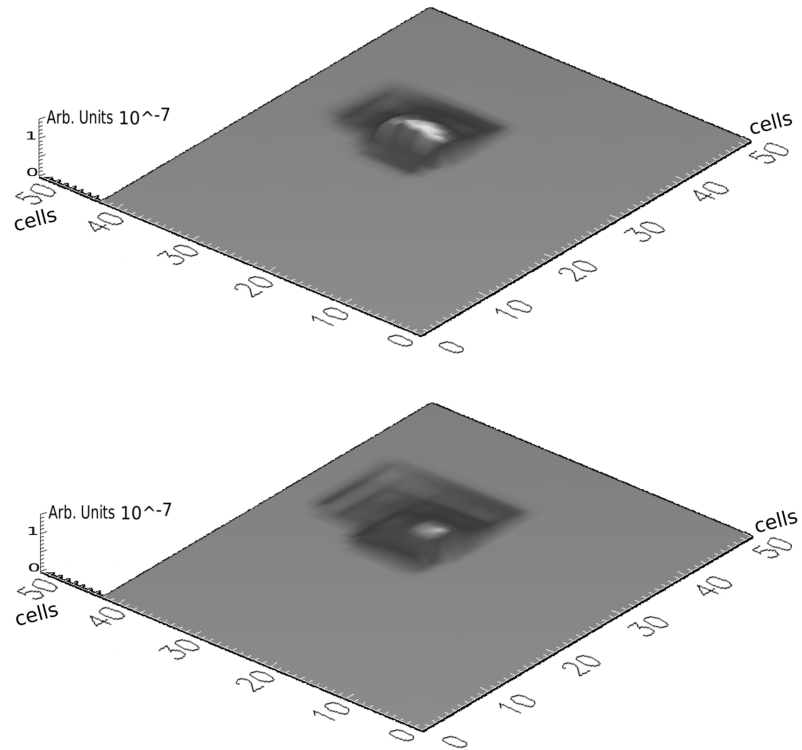


Figure 6. Synthetic model radio images of an approaching rectangular thin plasmoid. Top: the centre of the rectangle has more intensity than its edges, attributed to faster arrival of central rays compared to rays from the edges of the rectangle. The intensity peak is not fully symmetric within the inner rectangle, since the imaging focal point is not exactly on the plasmoid's trajectory. On the other hand, by setting a speed of light c to be much higher than normal (bottom), the effect largely vanishes. We can also see shadows of the central region and of the receding blob of the twin jet. Vertical scale for intensity is linear, in arbitrary units.

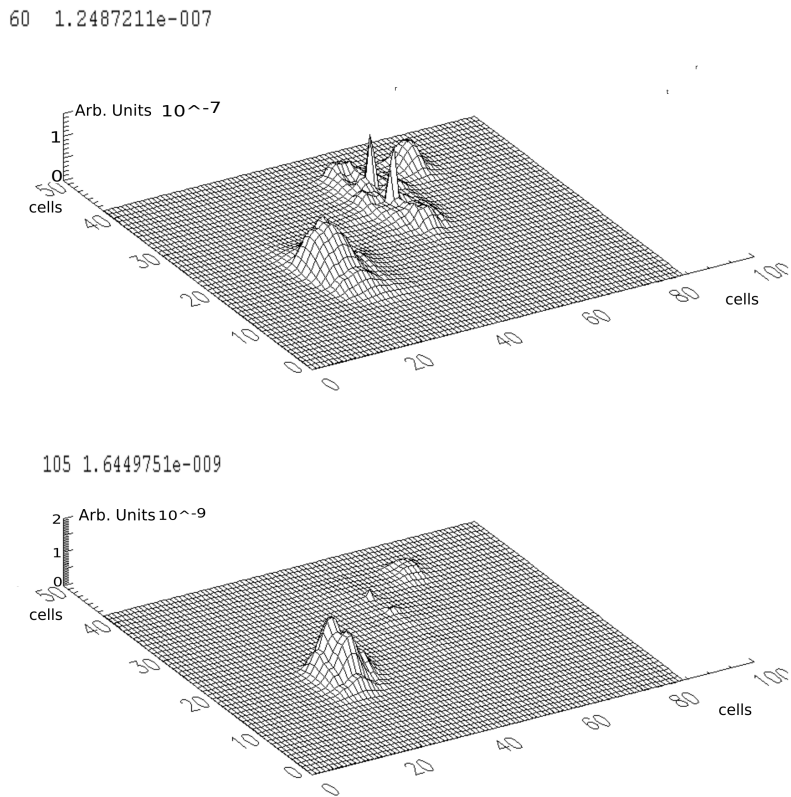


Figure 7. Unnormalized synthetic radio synchrotron images of the model system, at 8 GHz. Top, heavier jet model at snapshot 60 ($t=120$ ks). Bottom, lighter jet at snapshot 105 ($t=210$ ks). In both cases we can see blobs moving in diametrically opposite directions. A finite c is taken into consideration in these plots, resulting in the approaching blob apparently moving much faster than the receding one. Approaching plasmoid is also much brighter, even though in the hydrocode the blobs of each pair are essentially the same. Furthermore, the images shown here correspond to earlier blob locations in the hydrocode run, due to the delay in arrival of rays to the fiducial observer. Total intensity from the heavy model is roughly two orders of magnitude larger than the lighter one, in rough proportion to the ratio of jet nozzle densities for the two cases. A stronger equatorial emission appears in the heavy jet case, attributed to the higher densities of this run, as well as to the earlier timetag of the heavy model synthetic image.

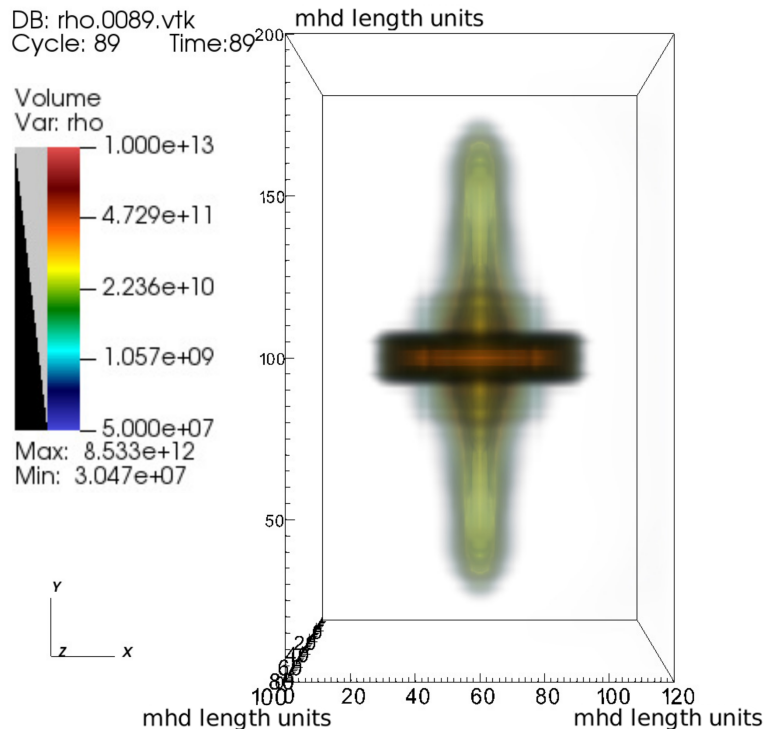


Figure 8. At the neutrino emission scale, a continuous jet is shown, traversing the heavier accretion disk wind construct, and also the companion’s stellar wind. Narrow collimated jets, lighter than inner winds, propagate first through the accretion disk wind and then the stellar wind, thus inflating a ‘composite’ cocoon structure. In the model, the accretion disk construct appears to divide the inner jet region into two separate dynamical environments, one for each jet. Furthermore, siderreal expansion of the inner part of the cocoon accrues enough dense and relatively fast matter, to achieve adequate (beamed, according to [37]) sideways neutrino emission, as seen in the synthetic neutrino images that follow later in this paper. The effects of the accretion disk and its wind construct therefore seem to play an important dynamical role in providing sideways particle emission from the jet system.

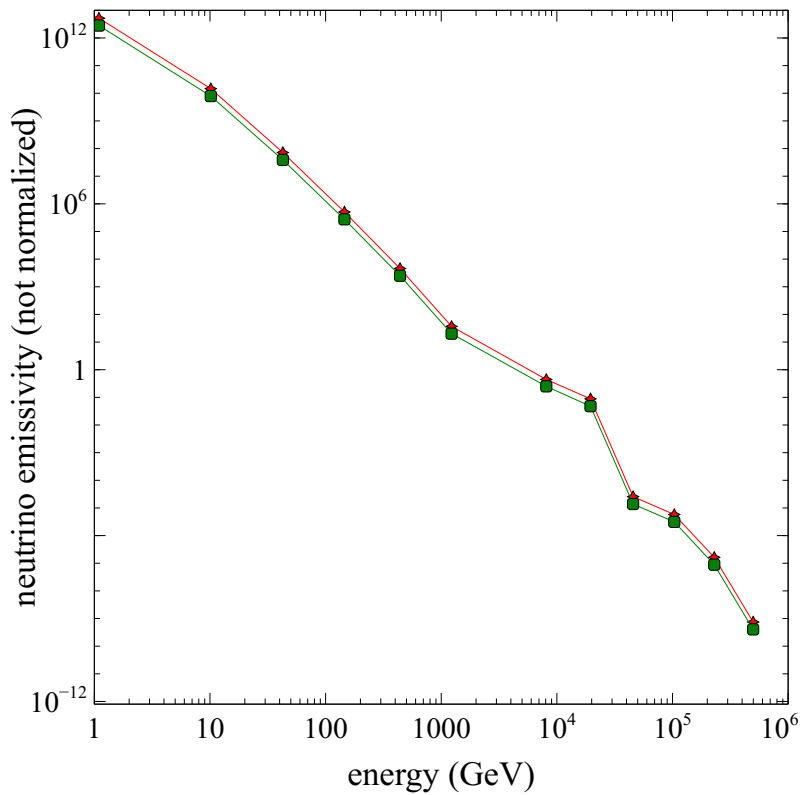


Figure 9. Neutrino unnormalized intensity plots, at snapshots 45 ($t=90$ s, top) and 90 ($t=180$ s, bottom). The sum of all pixels of the synthetic neutrino image at each energy, is plotted at each time instant. The finite nature of the speed of light is taken into account when calculating these plots. Intensity decreases with energy over an energy spectrum covering six orders of magnitude. We can see the intensity drop a little between the two instants. Still, spectra remain very similar in shape.

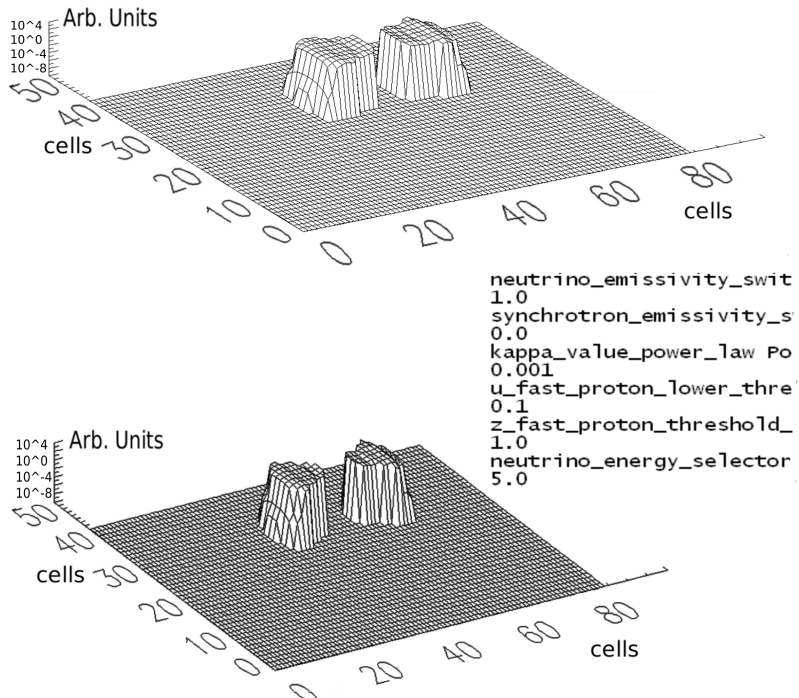


Figure 10. Unnormalized neutrino intensity images at two different times, same hydrocode run, snapshots 45 (top; $t = 90$ s) and 90 (bottom; $t = 180$ s), at a specific energy (400 GeV). In order to produce the image in rlos, the imaging method of a focused beam, with back in time integration along the LOS, was employed. In all other energy slots of the spectral energy distribution, image shape is quite similar, though not same, but intensity scale does fall with energy. Emission calculations are double filtered, by setting a maximum for the angle between local LOS and local u , and a minimum for local velocity.

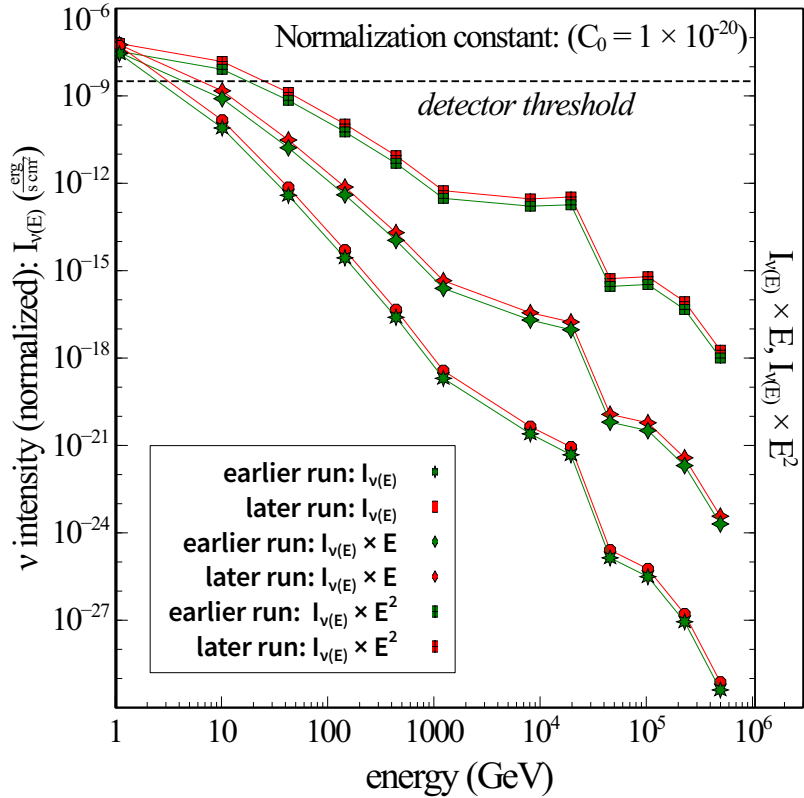


Figure 11. Neutrino normalized intensity spectral emission distribution plots, at snapshots 45 and 90 ($t=90$ s and 180 s, respectively). The synthetic imaging viewing angle of the model system, used to produce these spectra, is from the side, roughly perpendicular to the jets. Contribution to emission is then mostly from matter elements moving sideways, during jet cocoon expansion through ambient winds. Sizeable sideways emission does appear in the synthetic images, and that is reflected in the normalization process assumptions used here. We can also see the reference sensitivity of cubic km detector array.

As shown in [22], the scale of total emission is expected to increase the closer the LOS is to the approaching jet axis. Current results (Figure 11) demonstrate the possibility of potential observations, even when the jet is observed from the side. In other words, in this work beaming [37] is localized in cells whose relativistic speed points towards Earth, even though the jet axis lies essentially perpendicular to our line of sight. As a concrete example, the detection ability of cubic km array is depicted in the normalized SED plot, Figure 11, presenting a reasonable possibility for detection.

The above estimate may then be employed in order to provide a rough estimate of expected neutrino emission from a distribution of microquasars in the galaxy. The authors in [52] argued an estimated population of around a hundred systems in our galaxy. Furthermore, their discussion of γ ray emission from microquasars clarifies the importance of relativistic boosting in jet emission. Thus, orientation to Earth plays a major role here, and the situation is similar for neutrino emission [37].

For neutrino emission, in a manner similar to [22], we proceed by accepting 100 systems at various distances ranging from a minimum of 1 kpc to a maximum of 30 kpc, with average kinetic luminosity similar to our model system. The linear dependence of emissions on the latter quantity facilitates such a simplification. A distance of 1 kpc commands a flux at Earth of 25 times more than our model value, whereas the representative system situated at 30 kpc has 36 times less than at 5 kpc.

An orientation of less than 60 degrees might be 1 order of magnitude less than our value, but a jet system aimed towards us could perhaps have up to 100 times more visibility at Earth [22]. The latter point can be somehow altered by the present analysis, inasmuch as even from the side, expanding cocoons lead to local siderreal beaming

435 towards Earth. Orientation then remains the most important factor, but the low intensity
436 end of the range might be updated upwards, since local cell velocity might point towards
437 Earth even if the jet axis does not. Then we have distance and lastly jet kinetic power.
438 The latter order allows for an estimate of perhaps 5%, or five systems with a very high
439 relativistic boosting towards us, a number of maybe 40 or 50 at angles above 45 degrees,
440 and lastly maybe 50 at below 45 degrees, which still may have sizable contributions. The
441 first five probably contribute the most on average, and the ones viewed from the side
442 have a relatively smaller effect. A possible system located at a smaller distance, oriented
443 towards Earth, would of course dominate the above distribution, but the possibility for
444 such an occurrence is not very large.

445 On the basis of the above discussion, we then accept a rough average for a neutrino-
446 emitting galactic microquasar located at 15 kpc, with the kinetic luminosity of our model
447 (less affecting factor) and orientated at 37.5 degrees from the line of sight.

448 The reason for having the average angle 37.5 degrees, as compared to the 30 degrees
449 of [22], is the now higher contribution from systems not aimed towards us, due to
450 increased siderreal emission from dynamical jet systems.

451 The orientation of local velocity and magnetic field, seems to play a crucial role in
452 both neutrino and radio emission calculations. Consequently, differential projection at
453 each cell strongly affects final images.

454 It seems possible, even more than in [22], that the detection of background emission
455 from a potential distribution of microquasars in the galaxy lies within the realm of
456 modern detector arrays. This is also a consideration for the next generation of new or
457 upgraded arrays. On the other hand, a single X-ray binary system might act as a galactic
458 source of high-energy neutrinos. This is a potential target for a particle sensor with
459 increased angular accuracy. The variability of microquasars within the human timescale,
460 combined with their relative stability as a known point source, offers a good target for
461 observation, especially combined with sensors working in the electromagnetic spectrum.

462 *5.3. A conceptual link between electromagnetic and particle emissions from the jets*

463 Proposed neutrino emission from jets favours the presence of high energy protons
464 and electrons, triggering particle cascades that lead to neutrinos. Jets are therefore
465 acceleration sites, possibly at shock fronts inside them. High energy electrons lay the
466 foundation for synchrotron emission in the radio, as well as emission in other parts
467 of the electromagnetic spectrum. Shock front acceleration therefore energizes the jets,
468 leading to both particle and radiation production thereafter.

469 **6. Conclusions**

470 At the radio-scale model, there is apparent acceleration of the approaching plasmoid,
471 on the fiducial sky plane, as well as increased brightness. On the other hand, the receding
472 one appears to move slower, while also being dimmer. In the RMHD hydrocode model,
473 each pair of blobs are essentially identical, so the imaging model captures the apparent
474 relativistic acceleration and beaming, at each jet point. Furthermore, frequency shift
475 is also included, separately for each computational cell. This way, a more realistic
476 simulation of the model system observation is achieved, facilitating comparison with
477 observations. The dynamics in the hydrocode, and the magnetic fields threading the jets,
478 are then better connected to how the system actually appears to a detector array.

479 At the neutrino-scale model, an updated result is obtained, favouring sideways
480 emission from relativistic jets. This may lead to an increased number of MQ candidate
481 neutrino sources.

482 The method of synthetic imaging using special relativistic methodology, may be
483 expanded to a general relativistic framework. At every grid point, a gravitational
484 potential may alter the course of a ray, depending on local properties of matter and
485 energy, as provided by a suitable hydrocode simulation. This way, a broader range of
486 astrophysical problems can be approached, with increased realism. Particle emissions

487 can be included, if suitable transformation equations are provided for their energy
488 spectra, from the source reference system to a stationary one.

489 **Acknowledgements**

490 We are grateful to our colleagues for their valuable comments on the manuscript.
491 Special thanks go to Prof. G. E. Romero (UNLP, IAR) for his suggestions on improving
492 the content of this work.

- 493
- 494 1. Mirabel, I.F.; Rodríguez, L.F. *Ann. Rev. Astron. Astrophys.* **1999**, *37*, 409.
 - 495 2. Romero, G.E.; Torres, D.F.; Kaufman Bernadó, M.M.; Mirabel, I.F. Hadronic gamma-ray
496 emission from windy microquasars. *Astron. Astrophys.* **2003**, *410*, L1–L4, [[arXiv:astro-ph/astro-ph/0309123](#)]. doi:10.1051/0004-6361:20031314-1.
 - 497 3. Bednarek, W. TeV Neutrinos from Microquasars in Compact Massive Binaries. *Ap. J.* **2005**,
498 *631*, 466–470, [[arXiv:astro-ph/astro-ph/0505547](#)]. doi:10.1086/432411.
 - 499 4. Bosch-Ramon, V. Theoretical overview on high-energy emission in microquasars. *Astro-
500 physics and Space Science* **2007**, *309*, 321–331. doi:10.1007/s10509-007-9407-x.
 - 501 5. Reynoso, M.M.; Romero, G.E.; Christiansen, H.R. Production of gamma rays and neutrinos
502 in the dark jets of the microquasar SS433. *MNRAS* **2008**, *387*, 1745–1754, [[arXiv:astro-ph/0801.2903](#)]. doi:10.1111/j.1365-2966.2008.13364.x.
 - 503 6. Reynoso, M.M.; Romero, G.E. Magnetic field effects on neutrino production in micro-
504 quasars. *Astron. Astrophys.* **2009**, *493*, 1–11, [[arXiv:astro-ph/0811.1383](#)]. doi:10.1051/0004-
505 6361:200811004.
 - 506 7. Christiansen, H.R. High energy emission from galactic jets, 2013, [[arXiv:astro-ph.HE/1306.1792](#)].
 - 507 8. Zhang, J.F.; Feng, Y.G.; Lei, M.C.; Tang, Y.Y.; Tian, Y.P. High-energy neutrino emission from
508 low-mass microquasars. *MNRAS* **2010**, *407*, 2468–2474. doi:10.1111/j.1365-2966.2010.17072.x.
 - 509 9. Reynoso, M.M.; Carulli, A.M. On the possibilities of high-energy neutrino production in
510 the jets of microquasar SS433 in light of new observational data. *Astroparticle Physics* **2019**,
511 *109*, 25–32, [[arXiv:astro-ph.HE/1902.03861](#)]. doi:10.1016/j.astropartphys.2019.02.003.
 - 512 10. Carulli, A.M.; Reynoso, M.M.; Romero, G.E. Neutrino production in Population III mi-
513 croquasars. *Astroparticle Physics* **2021**, *128*, 102557, [[arXiv:astro-ph.HE/2101.02999](#)]. doi:
514 10.1016/j.astropartphys.2021.102557.
 - 515 11. Escobar, G.J.; Pellizza, L.J.; Romero, G.E. Highly collimated microquasar jets as efficient
516 cosmic-ray sources. *Astron. Astrophys.* **2022**, *665*, A145, [[arXiv:astro-ph.HE/2207.08633](#)]. doi:
517 10.1051/0004-6361/202142753.
 - 518 12. Gutiérrez, E.M.; Combi, L.; Romero, G.E.; Campanelli, M. Flares from dual jets in su-
519 permassive black hole binaries. *arXiv e-prints* **2023**, p. arXiv:2301.04280, [[arXiv:astro-
520 ph.HE/2301.04280](#)]. doi:10.48550/arXiv.2301.04280.
 - 521 13. Egron, E.; Rodriguez, J.; Trushkin, S.A.; Pellizzoni, A.; Pilia, M.; Melis, A.; Righini, S.; Bouchet,
522 T.; Cangemi, F.; Coleiro, A.; Chenevez, J.; Grinberg, V.; Loru, S.; Petrucci, P.O.; Pottschmidt,
523 K.; Steiner, J.; Tomsick, J.; Wilms, J.; Zhang, S.; Zhang, S.; Tao, L. A bright radio flare observed
524 in GRS 1915+105 with the Medicina and RATAN radio telescopes with no X-ray counterpart
525 in the INTEGRAL energy range. *The Astronomer's Telegram* **2023**, *16008*, 1.
 - 526 14. Koessl, D.; Mueller, E.; Hillebrandt, W. Numerical simulations of axially symmetric magne-
527 tized jets. I - The influence of equipartition magnetic fields. II - Apparent field structure and
528 theoretical radio maps. III - Collimation of underexpanded jets by magnetic fields. *Astron.
529 Astrophys.* **1990**, *229*, 378–415.
 - 530 15. Rieger, F.M.; Duffy, P. A Microscopic Analysis of Shear Acceleration. *Ap. J.* **2006**, *652*, 1044–
531 1049, [[arXiv:astro-ph/astro-ph/0610187](#)]. doi:10.1086/508056.
 - 532 16. Rieger, F.M. An Introduction to Particle Acceleration in Shearing Flows. *Galaxies* **2019**, *7*, 78,
533 [[arXiv:astro-ph.HE/1909.07237](#)]. doi:10.3390/galaxies7030078.
 - 534 17. Singh2019MHD. Study of relativistic magnetized outflows with relativistic equation
535 of state. *Monthly Notices of the Royal Astronomical Society* **2019**, *488*, 5713–5727,
536 [<https://academic.oup.com/mnras/article-pdf/488/4/5713/29191239/stz2101.pdf>].
537 doi:10.1093/mnras/stz2101.
 - 538 18. Hughes, P.A. In *Beams and Jets in Astrophysics*; Hughes., Ed.; Cambridge University Press,
539 1991.

- 542 19. Kelner, S.R.; Aharonian, F.A.; Bugayov, V.V. Energy spectra of gamma rays, electrons, and
543 neutrinos produced at proton-proton interactions in the very high energy regime. *Phys. Rev.*
544 *D* **2006**, *74*, 034018, [[arXiv:astro-ph/astro-ph/0606058](#)]. doi:10.1103/PhysRevD.74.034018.
- 545 20. Lipari, P.; Lusignoli, M.; Meloni, D. Flavor composition and energy spectrum of astrophysical
546 neutrinos. *Physical Review D* **2007**, *75*. doi:10.1103/physrevd.75.123005.
- 547 21. Pacholczyk, A.G. *Radio astrophysics. Nonthermal processes in galactic and extragalactic sources*;
548 1970.
- 549 22. Smponias, T. Synthetic Neutrino Imaging of a Microquasar. *Galaxies* **2021**, *9*, 80. doi:
550 10.3390/galaxies9040080.
- 551 23. Lampa, A. *Zeitschrift fur Physik* **1924**, *27*, 138.
- 552 24. Terrell, J. *Phys. Rev.* **1959**, *116*, 1041.
- 553 25. Penrose, R. *Proc. Cambridge Phil. Soc.* **1959**, *55*, 137.
- 554 26. Weisskopf, V.F. *Phys. Today* **1960**, *13*, 24.
- 555 27. Scott, G.D.; Viner, M.R. *American Journal of Physics* **1965**, *33*, 534.
- 556 28. Weiskopf, D. Dissertation. PhD thesis, Dissertation, der Eberhard-Karls-Universitat zu
557 Tubingen, der Fakultat fur Physik, 2001.
- 558 29. Deissler, R.J. *Am. J. Phys.* **2005**, *73*, 663.
- 559 30. Weiskopf, D. In *Scientific Visualization: Advanced Concepts*; Hagen, H., Ed.; Dagstuhl Publish-
560 ing, Leibniz Center for Informatics, Germany, 2010; p. 289–302.
- 561 31. Cawthorne, T.V. In *Beams and Jets in Astrophysics*; Hughes., Ed.; Cambridge University Press,
562 1991.
- 563 32. Weiskopf, D.; Kraus, U.; Ruder, H. *ACM Trans. Graph.* **1999**, *18*, 3.
- 564 33. Klauber, R.D. Is detection of Fitzgerald-Lorentz contraction possible? [arXiv:0808.1117v1](#).
- 565 34. Rybicki, G.B.; Lightman, A.P. *Radiative Processes in Astrophysics*; Wiley-Interscience: New
566 York, 1979.
- 567 35. Jarabo, A.; Masia, B.; Velten, A.; Barsi, C.; Raskar, R.; Gutierrez, D. *Computer Graphics Forum*,
568 *34* (8) **2015**, *34*, 1.
- 569 36. Hickey, F.R. *Am. J. Phys.* **1979**, *47*, 711.
- 570 37. Torres, D.F.; Reimer, A. Hadronic beam models for quasars and microquasars. *Astron.*
571 *Astrophys.* **2011**, *528*, L2, [[arXiv:astro-ph.HE/1102.0851](#)]. doi:10.1051/0004-6361/201116488.
- 572 38. Lobato, R.V.; Coelho, J.G.; Malheiro, M. Ultra-high energy cosmic rays from white dwarf
573 pulsars and the Hillas criterion. *Journal of Physics Conference Series*, 2017, Vol. 861, *Journal*
574 *of Physics Conference Series*, p. 012005, [[arXiv:astro-ph.HE/1703.06208](#)]. doi:10.1088/1742-
575 6596/861/1/012005.
- 576 39. Begelman, M.C.; Blandford, R.D.; Rees, M.J. Massive black hole binaries in active galactic
577 nuclei. *Nature* **1980**, *287*, 307–309. doi:10.1038/287307a0.
- 578 40. Romero, G.E.; Müller, A.L.; Roth, M. Particle acceleration in the superwinds of starburst
579 galaxies. *Astron. Astrophys.* **2018**, *616*, A57.
- 580 41. Derishev, E.V.; Aharonian, F.A.; Kocharyan, V.V. High-energy emission from off-axis
581 relativistic jets. *High Energy Gamma-Ray Astronomy*; Aharonian, F.A.; Völk, H.J.; Horns, D.,
582 Eds., 2005, Vol. 745, *American Institute of Physics Conference Series*, pp. 510–515, [[arXiv:astro-](#)
583 [ph/astro-ph/0501197](#)]. doi:10.1063/1.1878454.
- 584 42. Smponias, T.; Kosmas, O. *Advances in High Energy Physics* **2015**, 921757.
- 585 43. Smponias, T. RLOS: Time-resolved imaging of model astrophysical jets, 2018, [[1811.009](#)].
- 586 44. Smponias, T.; Kosmas, T.S. *MNRAS* **2011**, *412*, 1320.
- 587 45. Smponias, T.; Kosmas, T.S. *MNRAS* **2014**, *438*, 1014.
- 588 46. Kosmas, O.; Smponias, T. AHEP accepted.
- 589 47. Hjellming, R.M.; Johnston, K.J. *ApJ* **1988**, *328*, 600.
- 590 48. Mignone, A.; Bodo, G.; Massaglia, S.; Matsakos, T.; Tesileanu, O.; Zanni, C.; Ferrari, A. *Ap. J.*
591 *Supp.* **2007**, *170*, 228.
- 592 49. Smponias, T. nemiss: neutrino imaging of model astrophysical jets,
593 github.com/teoxxx/nemiss_pbl, 2019.
- 594 50. Fabrika, S. The jets and supercritical accretion disk in SS433. *2004*, *12*, 1–152, [[arXiv:astro-](#)
595 [ph/astro-ph/0603390](#)].
- 596 51. Kološ, M.; Tursunov, A.; Stuchlík, Z. Possible signature of the magnetic fields related to
597 quasi-periodic oscillations observed in microquasars. *The European Physical Journal C* **2017**,
598 *77*. doi:10.1140/epjc/s10052-017-5431-3.
- 599 52. Paredes, J.M.; Martí, J. Microquasars in the galaxy. *Contributions to Science* **2003**, *2*, 303–314.
- 600 53. Hsiung, P.; Dunn, R. *Proceedings of Supercomputing 1989 Conference* **1989**, *1*, 597.

- 601 54. Hsiung, P.; Thibadeau, R.; Wu, M. *Computer Graphics* **24**(2) **1990**, 24, 83.
 602 55. Kraus, U. *American Journal of Physics* **2000**, 68, 56.
 603 56. Muller, T.; Boblest, S. *Eur. J. Phys.* **2014**, 35, 06502.
 604 57. Muller, T. *Comput. Phys. Commun.* **2014**, 185, 2301.
 605 58. Velten, A.; Wu, D.; Jarabo, A.; Masia, B.; Barsi, C.; Joshi, C.; Lawson, E.; Bawendi, M.;
 606 Gutierrez, D.; Raskar, R. *ACM Trans. Graph.* **2013**, 32, 4.
 607 59. Sherin, Z.W.; Cheu, R.; Tan, P.; Kortemeyer, G. Visualizing Relativity: the OpenRelativity
 608 Project. *American Journal of Physics* **2016**, 84, 369.
 609 60. Sparks, W.B.; Fraix-Burnet, D.; Macchett, F.; Owen, F.N. A counterjet in the elliptical galaxy
 610 M87. *Nature* **1992**, 355, 804.
 611 61. Laing, R.; Bridle, A.H. Relativistic models and the jet velocity field in the radio galaxy 3C 31.
 612 *Monthly Notices of the Royal Astronomical Society* **2002**, 336, 328.
 613 62. Kortemeyer, G.; Tan, P.; Schirra, S. A Slower Speed of Light: Developing intuition about
 614 special relativity with games FDG 2013. *FDG '13 Proceedings of the International Conference on*
 615 *the Foundations of Digital Games*. ACM New York, NY, USA **2013**, 1, 400.
 616 63. Kosmas, O.; Smponias, T. Simulations of Gamma-ray emission from magnetized micro-
 617 quasar jets. *arXiv e-prints* **2018**, p. arXiv:1808.00303, [[arXiv:astro-ph.HE/1808.00303](https://arxiv.org/abs/1808.00303)].
 618 64. Smponias, T.; Kosmas, O. *Advances in High Energy Physics* **2017**, 4962741.
 619 65. Campion, S.; Fuksman, J.D.M.; Hernandez, J.A.R. Neutrino production from proton-proton
 620 interactions in binary-driven hypernovae, 2020, [[arXiv:astro-ph.HE/1910.10439](https://arxiv.org/abs/1910.10439)].
 621 66. Purmohammad, D.; Samimi, J. On the hadronic beam model of TeV gamma-ray flares from
 622 blazars. *Astron. Astrophys.* **2001**, 371, 61–67. doi:10.1051/0004-6361:20010308.

623 7. Appendix 1

624 7.1. Model space size

625 The computational grid size is $l_{\text{grid}} = 200 \times 10^{13} \text{ cm} = 2 \times 10^{15} \text{ cm}$. Distance to
 626 the generic MQ model system is taken as $D = 5 \text{ kpc}$, or $D \simeq 1.5 \times 10^{22} \text{ cm}$. Therefore,
 627 $\sin(\frac{l_{\text{grid}}}{D}) \simeq 1.3 \times 10^{-7}$. For such small angles, $\sin(\text{angle}) \simeq \text{angle}$. Thus, arc size is around
 628 $1.3 \times 10^{-7} \text{ rad}$, or roughly 27 mas. The latter size is for the full computational domain,
 629 including jet and counterjet, as well as certain empty space margin. Consequently, for
 630 the core of the model grid, the model jet and counter-jet region spans no more than
 631 perhaps 15 mas. We may then consider a synchrotron emission region of up to 10 mas
 632 for a model jet, which is generally thought to be the inner compact region, where a flat
 633 to inverted spectrum may occur.

634 7.2. Normalization

635 The jet kinetic energy at its base is [6]

$$E_k = \frac{1}{2}(\Gamma m)u^2 \quad (9)$$

where u is jet speed, Γ is Lorentz factor and m the mass of a jet portion traversing a jet cross section near the base. Then, jet kinetic power P_k is the kinetic energy traversing the cross section per unit time

$$P_k = dE_k/dt = \frac{1}{2}(\Gamma dm/dt)u^2 \quad (10)$$

where the speed is taken to be constant during an ejection episode (it was also set to be constant in the simulation described here). However,

$$dm/dt = \rho dV/dt = \rho Adx/dt = \rho Au \quad (11)$$

where ρ is jet density, V is the volume of a thin jet cross section, of length dx , near the jet base, and A is the jet base cross section area, also taken as a constant both in the simulation and here. Therefore,

$$P_k = dE_k/dt = \frac{1}{2}(\Gamma \rho A)u^3 \quad (12)$$

or

$$P_k = dE_k/dt = \frac{1}{2}(\Gamma\rho N_{\text{cell}}L_{\text{cell}}^2)u^3 \quad (13)$$

636 where $A = N_{\text{cell}}L_{\text{cell}}^2$ is the area of jet cross section near the base, L_{cell} is the length of the
 637 edges of a cubical computational cell, at the jet base, L_{cell}^2 is the frontal area of a cell, and
 638 N_{cell} is the number of such cells forming the jet base cross section.

We then express density as a function of proton number density N_p and proton mass m_p

$$\rho = N_p m_p. \quad (14)$$

639 The field of view (FOV) of the synthetic image is taken at an estimated 1/10 of
 640 the total solid angle. In there, a similar portion of total emission is assumed, allowing
 641 for the majority of emission to go in the vicinity of the jet axis orientation. In total, a
 642 field-of-view factor of 1/100 of total emmission is employed: $f_{\text{fov}}=0.01$.

643 For the neutrino-scale model, let us define neutrino luminosity L_ν as the power
 644 emitted through neutrinos from the jet, which is a fraction α of the total kinetic jet power
 645 (jet kinetic luminosity $P_k=L_k$).

646 Consequently, $\alpha = L_\nu/L_k$, representing the portion of jet power emitted in neutrinos.
 647 For normalisation, a working value is taken as 10^{-3} . This can be justified from a
 648 $q_{\text{rel}}=0.1$ for the energy content of the relativistic particles in the jet [6], [9], on top of which
 649 we employ the efficiency of the cascade when transferring energy from hot protons to
 650 final neutrinos.

651 The shape of the spectrum is also affected by acceleration efficiency [9], and from
 652 the opening angle of the jet [6], thus affecting the area under the neutrino spectrum plot.
 653 As an approximation for the above effects, we adopted a value of 0.01 for the energy
 654 transfer from nonthermal protons to the neutrinos.

We also set $u = \beta c$. A less-than-unity positive filtering factor f_f is employed that accounts for not using all jet cells, but only those with velocity orientation closer to the LOS and with speed above a given limit. We then have

$$L_\nu = \alpha L_k = \alpha P_k = \alpha dE_k/dt = f_{\text{fov}}f_f \frac{1}{2}\alpha\Gamma(N_p m_p N_{\text{cell}} L_{\text{cell}}^2) \beta^3 c^3 \quad (15)$$

The intensity of the jet is then expressed as $I_\nu = L_\nu/4\pi D^2$, where D is the distance to Earth. Thus,

$$I_\nu = f_{\text{fov}}f_f \frac{1}{4\pi D^2} \alpha \frac{1}{2} \Gamma(N_p m_p N_{\text{cell}} L_{\text{cell}}^2) \beta^3 c^3 \quad (16)$$

655 In the neutrino-scale simulation, the jet beam travels at $\beta=\frac{u}{c}=0.8$, with a density of
 656 10^{11} protons/cm³. L_{cell} is 10^{10} cm, while the number of cells comprising the beam at its
 657 base at this resolution is $N_{\text{cell}} \simeq 15$. Distance to Earth is taken here with a typical value
 658 of $D = 5$ kpc or approximately 2×10^{22} cm.

We then integrate the area under the curve of the arbitrary units plot (Figure 9) for our case of viewing the jet from the side. That case is supposed, for the purposes of normalization, to be the one matching the orientation of the hypothetical system in relation to Earth. We perform a cumulative sum over the roughly 10 points. Thus, we find about 10^{11} , in arbitrary units (AU)*GeV. We replace an AU with a constant C_0 , so that $\text{AU}=C_0 \text{ erg}/(\text{s} \cdot \text{cm}^2)$. We set $I_\nu=L_\nu/4\pi D^2$ equal to the area under the plot of Figure 9, expressed in units of C_0 , in order to find the latter (normalization constant)

$$I^\circ = f_{\text{fov}}f_f \frac{1}{4\pi D^2} \alpha \frac{1}{2} (\Gamma(N_p m_p) N_{\text{cell}} L_{\text{cell}}^2) \beta^3 c^3 = (\text{PLOTAREA}) * C_0 \text{ erg}/(\text{s} \cdot \text{cm}^2) \text{ GeV} \quad (17)$$

659 For our case, we find $C_0 \simeq 10^{-20}$, which is the value of the arbitrary unit C_0 . Using
 660 the above constant, we multiply by it the value given in arbitrary units for the particle
 661 emission. Thus, the intensity plot is multiplied, and we arrive to the updated plot in
 662 Figure 11, which may be directly compared to other models and to observations.

663 For the radio-scale model, we may consider an estimate of the intensity in radio at
 664 8 GHz. Relativistic beaming is now present, for the E/M radiation. In a manner similar
 665 to particles (see above), beaming leads to an approximate value for the field of view
 666 factor of $f_{\text{fov}}=0.01$. The portion of the jet kinetic power L_k , emitted at the band in 8 GHz
 667 is estimated as PORTION. Therefore, our image includes $(1/30)*(\text{PORTION})*(L_k)$. On
 668 Earth, we use $D=5$ kpc and final intensity on Earth is the above divided by $(4\pi D^2)$.

669 8. Appendix 2

The equipartition calculation follows. As shown above, jet kinetic power is

$$670 \quad L_k = \frac{1}{2} \frac{dm}{dt} u^2 = \frac{1}{2} (\rho A u) u^2 = \frac{1}{2} \rho A u^3 \quad (18)$$

where $\frac{dm}{dt} = \rho \frac{dV}{dt} = \rho A \frac{dx}{dt} = \rho A u$
 Kinetic energy density is [6]

$$\rho_k = \frac{L_k}{\pi R_j^2 u_j} = \frac{L_k}{A u} = \frac{\frac{1}{2} \rho A u^3}{A u} = \frac{1}{2} \rho u^2, \quad (19)$$

At the nozzle, for the v -scale model, $\rho_k \simeq 1 \times 10^8 \text{ ergcm}^{-3}$. For the heavier jet radio-scale model, $\rho_k \simeq 1 \times 10^9 \text{ ergcm}^{-3}$ ($3 \times 10^8 \text{ ergcm}^{-3}$ temporal average due to intermittent jet), and for the lighter jet radio-scale model, $\rho_k \simeq 1 \times 10^7 \text{ ergcm}^{-3}$ ($3 \times 10^6 \text{ ergcm}^{-3}$ average).

Also

$$B = \sqrt{8\pi\rho_B} \quad (20)$$

and

$$\rho_B = B^2 / 8\pi \quad (21)$$

For both radio models, $\rho_B \simeq 10$. For the v -scale model, $\rho_B \simeq 10^7$. For equipartition, the kinetic and magnetic energy densities have to be equal to each other, $\rho_k = \rho_B$. Thus, both radio models have kinetic energy density higher than equipartition, whereas the v -scale model roughly fulfills the equipartition assumption.

678 9. Appendix 3

Additional properties of rlos imaging code are described here.

680 9.1. Theoretical background for imaging code

[53,54] provide an early computerized attempt to reconstruct a relativistic image, through the eyes of an observer crossing a scene at high velocity. [55] demonstrates the importance of the relativistic transform of brightness and color. When imaging a jet, these correspond to Doppler boosting and frequency shift, respectively. [55] discusses an object that moves at uniform speed across the field of view, but is visually large enough for the angle between velocity and line of sight to vary along the object. Applying the Lorentz transform changes brightness and color in a separate manner, for each point of the observed object. [28] improves on such calculations, providing various methods for relativistic visualization, in both Special and General relativistic frameworks.

[56] calculate the visual appearance of wireframe relativistic objects, by mathematically inverting the course of light, from an image point to the emission event. They provide expressions that directly describe how a series of objects would look like, when moving at high speed, in front of a stationary observer. The efficiency of their method is then compared to the increased detail of a related ray-tracing project [57]. [35] image scenes with a fast observer traveling through their artificial environment. They also relate their simulations to actual imaging experiments, using the femto-photography technique [58]. Furthermore, they introduce a number of additional details into their models, such as camera distortions from traveling at very high speed. [59] present a framework, where the subject of relativistic imaging is explored, in an accessible manner.

700 9.2. Time-resolved imaging

701 9.2.1. Accessing 4-dimensional data

702 The finite nature of the speed of light crucially affects the appearance of a fast-
703 moving object. Consequently, drawing a relativistic image of an astrophysical system,
704 necessitates the availability of information regarding both its spatial properties and its
705 temporal evolution. In the present case, when executing the hydrocode, before running
706 rlos, the temporal density of snapshots to be saved to disk at regular intervals, was
707 suitably adjusted. The smaller those intervals are, the better the temporal resolution of
708 hydrocode data is. A series of snapshots are then loaded to RAM by rlos, which thereby
709 requires more memory in order to run properly than the hydrocode itself does. Time
710 is measured in simulation time units, which are read by PLUTO's attached pload.pro
711 routine, which loads data into rlos.

712 The total time span available to an LOS, $\Delta t_{\text{LOS}(\text{total})} = t_{(\text{last-shot})} - t_{(\text{first-shot})}$ ⁴ (as
713 measured in simulation time units, not merely in number of snapshots) should be preset
714 to be larger than light crossing time of the model system, for the selected LOS angle
715 settings. Documenting model jet evolution generally requires hydrocode data saves to
716 be rather dense in time, especially for fast-changing flows. On the other hand, a lower
717 temporal resolution probably suffices for a steadier, slower-paced flow.

718 9.2.2. Traversing 4D arrays

719 Introduction

720 A series of hydrocode snapshots are loaded to RAM, populating the elements of
721 4-dimensional (4D) arrays. Let us examine the case of backwards in time imaging calcu-
722 lation. From a temporal point of view, we begin from the simulation time corresponding
723 to the last of the loaded snapshots, called shotmax. From a spatial point of view, we
724 start at a point of the imaging plane, which is a side of the computational box (Figure
725 1). As the calculation advances, in 3D space along the LOS being drawn (Figure 12), the
726 algorithm keeps checking whether to jump to a previous temporal slice while staying on
727 target in 3D (Figure 13). Consequently, the LOS advances back in time through data by
728 accessing different instants from the 4D data arrays. As a test case, the LOS may also be
729 set to advance forward in time, beginning from the time tag of shotmin, the first of the
730 loaded snapshots (Figure 13, 14).

⁴ Not to be confused with interval Δt_{shot} between successive snapshots

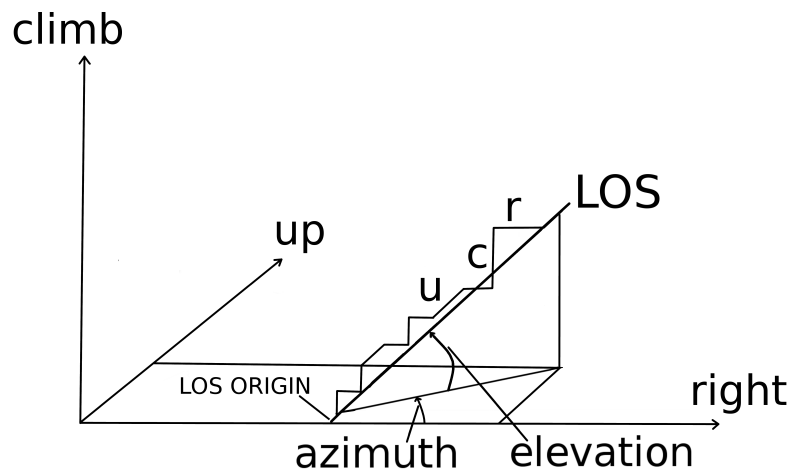


Figure 12. Schematic of the spatial propagation of a line of sight (LOS) through a 3D Cartesian computational grid. In the discrete grid, according to the design of the algorithm, there are 3 available directions to be taken at each step along the LOS: *right*, *up*, and *climb*. These correspond to *x*, *y*, and *z*, respectively. During propagation, the LOS tries to follow its given direction, as defined by the two angles of azimuth and elevation. More specifically, every two steps, a decision is first made on azimuth, either *right* or *up*. Then, for elevation, it is either *climb* or another azimuth decision. Along the LOS, horizontal steps point to the '*right*' direction. Diagonal steps represent going '*up*', while vertical ones constitute '*climb*' steps.

731 Time-resolved imaging calculations

732 For every LOS, there is a point of origin (POO), located on the imaging side of
 733 the computational grid (Figure 1). That point, addressed in rlos code as $(nx10, ny10,$
 734 $nz10)$ and here as O' , is the beginning of the LOS's axes x', y', z' , parallel to x, y , and z ,
 735 respectively. A 2D loop covers the imaging surface, the POO successively locating itself
 736 at each of the latter's points.

737 As we progress along an LOS, a record is kept of where we are, in 3D space. This
 738 record comprises the LOS's own integer coordinates, rc , uc , and cc , measured in cells,
 739 starting from its POO. The above symbols stand for right-current, up-current, and climb-
 740 current, representing the current LOS advance in the x' , y' , and z' axes, respectively
 741 (Figures 1 and 12). The current ray position is then $(nx10 + rc, ny10 + uc, nz10 + cc)$.

742 A timer variable, $curtime$ (standing for current LOS time), is introduced for each
 743 LOS, recording the duration of inssofar ray travel along the LOS. The aforementioned
 744 timer is preset at the beginning of each LOS to the hydrocode time of the first loaded data
 745 snapshot (forward in time integration), or of the last snapshot (back in time integration).
 746 For backwards in time ray-tracing, the above duration is subtracted each time from
 747 $t(shotmax)$.

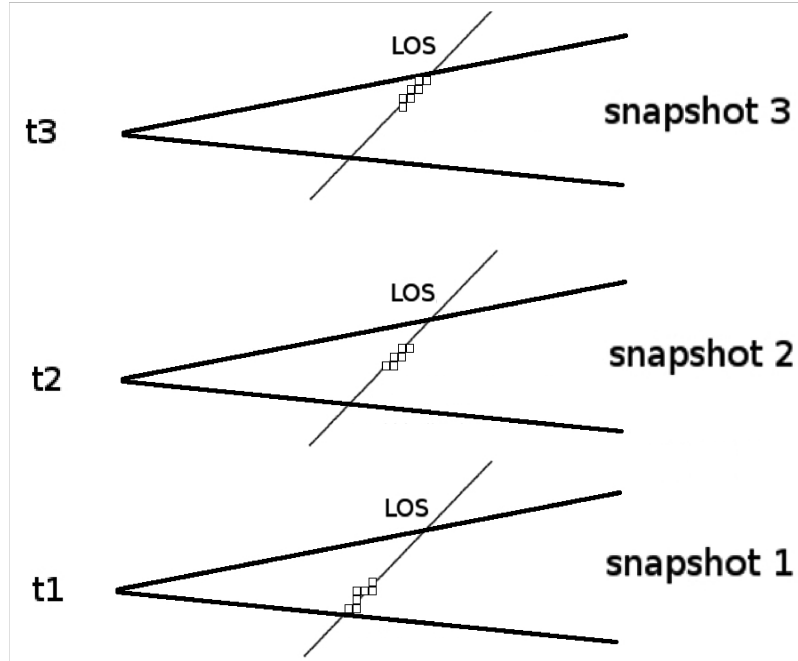


Figure 13. Three successive instants of a line of sight traversing a jet. At regular intervals, we jump to a new 3D slice of a 4D spacetime array, obtaining a discrete approximation of the time continuum in the form of hydrocode snapshots. The calculation may proceed either forward in time (from bottom to top) or backwards in time (from top to bottom).

⁷⁴⁸ We then proceed to calculate the current length of the LOS

$$l_{\text{los}(\text{current})} = [(dlr * (\text{nx1current} - \text{nx10}))^2 + (dlu * (\text{ny1current} - \text{ny10}))^2 + (dlc * (\text{nz1current} - \text{nz10}))^2]^{1/2} \quad (22)$$

where LOS length is measured in cell length units and

$$\text{nx1current} = \text{nx10} + \text{rc}, \text{ny1current} = \text{ny10} + \text{uc}, \text{nz1current} = \text{nz10} + \text{cc} \quad (23)$$

⁷⁴⁹ along the x, y, and z directions, dlc, dlu, and dlr are the respective *normalized* hydrocode
⁷⁵⁰ Cartesian cell lengths. Their values are usually unity or close to unity, as set in the
⁷⁵¹ hydrocode by the user, and rlos requires them fixed, meaning only homogeneous grids
⁷⁵² are currently supported. Furthermore, if the hydrocode grid is read by pload at a reduced
⁷⁵³ resolution, rlos cell sizes are automatically adjusted accordingly.

We can finally write

$$l_{\text{los}(\text{current})} = [((dlr * \text{rc})^2) + ((dlu * \text{uc})^2) + ((dlc * \text{cc})^2)]^{1/2} \quad (24)$$

We then proceed to calculate curtime, the current hydrosimulation time of the light ray along the LOS. For forward in time LOS advance

$$\text{curtime} = l_{\text{los}(\text{current})} / c_{\text{light}} + t_{\text{shotmin}}. \quad (25)$$

while for back in time ray-tracing

$$\text{curtime} = +t_{\text{shotmax}} - l_{\text{los}(\text{current})} / c_{\text{light}}. \quad (26)$$

⁷⁵⁴ t_{shotmin} is the timestamp of the first loaded snapshot, t_{shotmax} the one of the last snapshot
⁷⁵⁵ loaded, and clight is the speed of light in cells per simulation second.

756 When curtime crosses a new snapshot's time tag, the algorithm switches to drawing
757 the LOS through the 3D volume of the new snapshot (Figure 13). We keep moving along
758 the same LOS in 3D space, but we switch to a new time instant in the data. The above
759 temporal shift is repeated as many times as required by the relevant criterion along the
760 LOS until the spatial end of the LOS.

761 9.2.3. Aiming at the line of sight

762 The direction of an LOS in 3D space is defined by the two angles of azimuth (angle
763 1) and elevation (angle 2) (Figure 1), where the plane of angle 1 is the $x'y'$ plane, parallel
764 to xy .

765 LOS's may be either parallel to each other, or focused. With a focused beam, the
766 image is formed on a adjustable size fiducial screen located at a user-defined position
767 between the focal point and the model system (Figure 17).

768 For a jet parallel to the y axis, the angle between local jet matter velocity \vec{u} and LOS,
769 $\text{losu} = (\vec{L}\vec{O}\vec{S}, \vec{u})$, is generally small when angle 1 (xy azimuth) approaches 90 degrees
770 and vice versa (Figure 15). As is well-known [18], the angle losu affects the relativistic
771 emission calculations.⁵

772 For a jet along the y axis, the plane of angle 2 (elevation) is largely perpendicular to
773 the jet when azimuth (angle 1) is zero, while it is roughly parallel to the jet when azimuth
774 (angle 1) is 90 degrees. Usually, the jet bears an approximate cylindrical symmetry, and
775 this has an interesting effect on the sensitivity of the synthetic image to the viewing
776 angles (Figure 15). More specifically, for a small azimuth (angle 1), if we vary elevation
777 (angle 2), we indeed rotate the viewing point around the jet axis, thus producing similar
778 intensities, thanks to the approximate cylindrical symmetry of the jet. Thus, for a jet
779 moving along the y axis, the smaller azimuth (angle 1) is, the less difference varying
780 elevation (angle 2) makes.

781 On the other hand, for azimuth (angle 1) nearing $\pi/2$, varying elevation (angle 2)
782 rotates the view within a plane approximately parallel to the jet, resulting to considerable
783 differences in the image (no symmetry involved this time). Consequently, the larger
784 azimuth (angle 1) is, the stronger the effect, on the synthetic image, from changing
785 elevation (angle 2).

⁵ Individual jet elements maay still move in directions different than the main jet axis, as part of a dynamic flow.

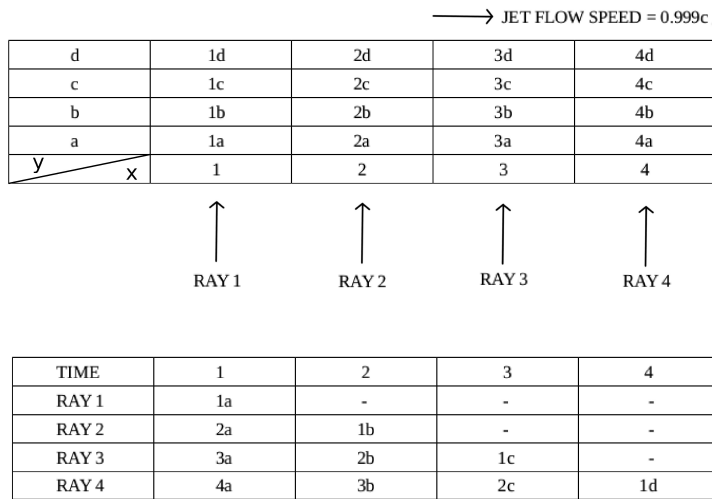


Figure 14. Simultaneous advance in two-dimensional space and forward in time of a few lines of sight. Top half depicts the spatial situation at $t = 1$. Sixteen jet matter portions occupy this mini 4 by 4 grid. Each piece of matter is named after its position at $t = 1$ and retains that name as it moves along. Bottom half shows how the situation evolves as time marches on, with light rays meeting different jet segments that cross their path. A dash means a light ray meeting jet matter other than the above or nothing at all.

786 9.3. *Relativistic Effects-Doppler boosting*

787 9.3.1. General

788 The main effects of the Lorentz/Poincaré transform on the emission from a rela-
 789 tivistic object [28], specifically applied to an astrophysical jet, are relativistic aberration,
 790 time dilation, and frequency shift [18,31,60,61].

This area refers to E/M emission, but not to particle emission. Jet spectrum is given by any suitable form inserted into the model, including the spectrum resulting from synchrotron emission and absorption coefficients. Earth frame jet spectrum S_{obs} can be expressed [18,31] as

$$S_{\text{obs}} = S_{\text{jet}} D^{3+\alpha} \quad (27)$$

791 where α is the spectral index and D is the Doppler factor. Exponent $(3+\alpha)$ in the above
 792 can be broken down into different contributions from separate effects. Two units come
 793 from the aberration of light, one from the relativistic dilation of time and α from the
 794 effect of frequency shift, while for a continuous optically thin jet, a D factor is lost [31].

795 Aberration-searchlight effect

796 Relativistic aberration changes the perceived direction of light (there is no ray
 797 curving in special relativity) when transforming between the jet frame and the earth
 798 frame, 'tilting rays' emanating from the jet, generally towards its head area.

799 At an individual cell level, cell emission along a ray *within* the cell's boost cone
 800 is then accordingly reinforced; if *outside* the cone, it is weakened. Depending on local
 801 velocity value and direction, neighbouring cells may have totally different boost cones.

802 Time dilation

803 Time dilation contributes one D factor to the emission result. Again, this refers to
 804 E/M radiation.

805 Frequency Shift

E/M radiation emitted at a given frequency, from fast-moving jet matter, is taken to be Doppler shifted in frequency

$$f_{\text{obs}} = f_{\text{calc}} D \quad (28)$$

806 where f_{obs} is the observed frequency, and f_{calc} is the frequency used in emission calcula-
807 tions performed in the jet frame of reference [18].

808 For $D \geq 1$, emission is calculated at a frequency lower than the observed, resulting
809 in higher intensity, when the employed spectrum decreases with frequency. For radio
810 emission, we therefore calculate emission and absorption at the $f_{\text{calc}}=f_{\text{obs}}/D$. Each
811 computational cell, in general, has its own Doppler factor D, and therefore its own
812 frequency shift.

813 9.3.2. Lorentz factor

814 The Lorentz factor for a hydrocode cell is [18]

$$\Gamma_{\text{Lorentz}} = \frac{1}{\sqrt{1 - u^2}} \quad (29)$$

where

$$u = \sqrt{u_x^2 + u_y^2 + u_z^2} \leq 1 \quad (30)$$

815 is the value of local velocity $\vec{u} = (u_x, u_y, u_z)$, in units of the speed of light.

816 9.3.3. Doppler factor calculation

Jet radiation is either boosted or deboosted, depending on the angle 'losu' between
the direction of the LOS and \vec{u} . The higher the jet speed is, the narrower and stronger the
cell boost cones are, around the direction of local velocity. On the other hand, outside
cell boost cones, deboosting occurs, that is to say, the higher the velocity is, the weaker
the signal becomes. D equals

$$D = \frac{\sqrt{1 - u^2}}{(1 - u * \cos(\text{losu}))} \quad (31)$$

817 For the above, the angle between the LOS and the local velocity vector is required
818 at every point of the computational space.

819 (As a note, for particles, their distribution is transformed to the Earth frame, as
820 shown in [37].)

821 The cosine of angle losu is calculated in the following manner:

Let us define a fiducial unitary LOS vector $(\vec{\text{LOS}}) = (lx_1, lx_2, lx_3)$, with $(\text{LOS}) = \sqrt{lx_1^2 + lx_2^2 + lx_3^2} = 1$. In the following, ϕ_1 and ϕ_2 represent azimuth and elevation angles
1 and 2, respectively.

$$lx_1 = \cos(\phi_1) \cos(\phi_2), \quad lx_2 = \sin(\phi_1) \cos(\phi_2), \quad lx_3 = \sin(\phi_2) \quad (32)$$

$$\vec{\text{LOS}} * \vec{u} = (\text{LOS}) \mathbf{u} \cos(\widehat{\vec{\text{LOS}}, \vec{u}}) = lx_1 u_x + lx_2 u_y + lx_3 u_z \quad (33)$$

Therefore, we have $((\text{LOS})=1)$

$$\cos(\widehat{\vec{\text{LOS}}, \vec{u}}) = \frac{lx_1 u_x + lx_2 u_y + lx_3 u_z}{(\text{LOS}) \mathbf{u}} = \frac{lx_1 u_x + lx_2 u_y + lx_3 u_z}{\sqrt{(u_x^2 + u_y^2 + u_z^2)}} \quad (34)$$

822 For back in time ray-tracing, a minus sign is introduced to the above equation. Fur-
823 thermore, a minuscule number is added to the denominator of Equation 34, in case $u =$
824 0. The above calculation allows the assignment of a Doppler boosting factor through
825 Equations 30, 31, and 34 to each discrete emission event along a line of sight.

826 9.3.4. CoslosB calculation

827 The calculation of the angle losb between the magnetic field and the LOS is per-
828 formed, in rlos, in exactly the same way as for losu, above. Only this time the vector of
829 velocity is replaced by the magnetic field one.

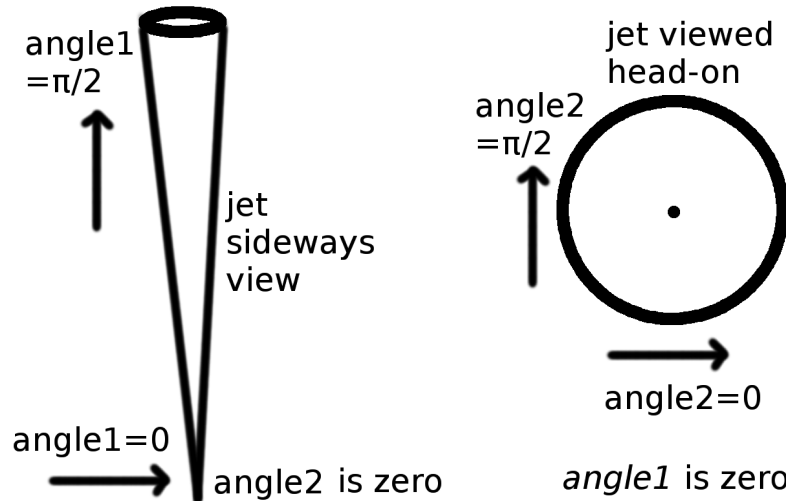


Figure 15. Geometric arrangement with regard to the viewing angles in the model for the special cases of $\text{angle2} = 0$ (left) and $\text{angle1} = 0$ (right). For each subcase, the arrow shows the LOS direction, which is different than the reader's direction of view.

830 Alternative frequency shift

831 rlos may include different emission dependencies on frequency, where we calculate
832 intensity at f_{calc} and observe that at f_{obs} .

833 *9.4. Testing parameters*

834 Certain parameters, that facilitate testing rlos, are presented here.

835 *9.4.1. The clight parameter*

836 Let us consider a 4D array, comprising a succession of hydrocode snapshots. The
837 LOS traversing those data, moves at a speed of clight cells per time unit. When we
838 artificially adjust clight to a lower value [59,62], then the algorithm jumps to a new
839 snapshot after spatially advancing through fewer cells. A slower LOS advances farther
840 in time while crossing a given distance through the jet, allowing for a detailed study of
841 the time-jumping algorithm. On the other hand, setting clight to a very high value leads
842 to a single shot image, as we never advance to a further temporal slice.

A representative hydrocode scaling is the following (for neutrinos)

$$L_{\text{sim}} = 10^{10} \text{ cm}, u_{\text{sim}} = 3 \cdot 10^{10} \frac{\text{cm}}{\text{s}}, \rho_{\text{sim}} = 1.67 \cdot 10^{-24} \frac{\text{g}}{\text{cm}^3}, t_{\text{sim}} = \frac{L_{\text{sim}}}{u_{\text{sim}}} = \frac{1}{3} \text{ s} \quad (35)$$

843 where t_{sim} is the hydrocode time unit, u_{sim} is the speed of light and L_{sim} is the hydrocode
844 length unit. When preparing the hydrocode run, the time span, in simulation seconds,
845 between data snapshots, should optimally be set, to $l_{\text{LOS}}/(n^* \text{clight})$. l is the LOS length,
846 in *cells* and n is the desired number of snapshots to cover the imaged timespan. If we
847 employ the parameter sfactor, pload's shrink factor, cells are enlarged and the calculated
848 value of clight shrinks accordingly (sfactor regrids the hydrodata to a coarser grid).
849 Overall accuracy then suffers somewhat, and shrinking the grid should be used only as
850 a preview.

851 Altering clight only affects the light ray speed, not the speed of matter. Conse-
852 quently, overriding clight does not affect the relativistic emission calculations (like
853 tweakspeed does, Section 9.4.4). An altered clight is merely an artifice, introduced in
854 post processing, in order to explore the effect of using more, or less, temporal slices in
855 the final image.

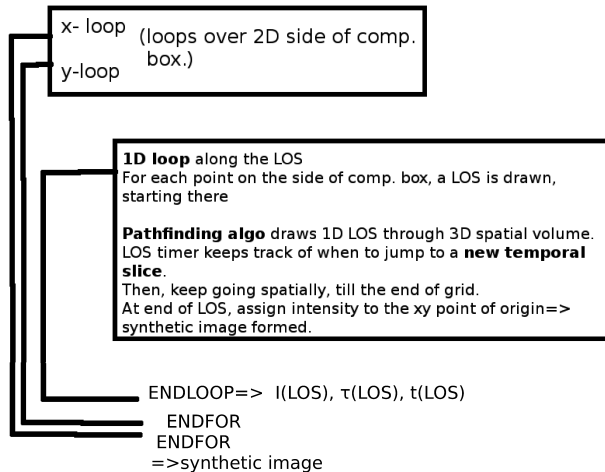


Figure 16. A simplified flow diagram depicting the basic logical structure of rlos imaging code, for the case of rays parallel to each other. The synthetic image's xy loops here correspond to either the yz or the xz side plane of the computational box.

856 9.4.2. The FS switch

857 After the hydrodata are loaded, a global operation calculates, for each cell, a jet
 858 frame frequency f_{calc} : $f_{\text{calc}} = f_{\text{obs}} / D$, where f_{obs} is the observing frequency and D is the
 859 local Doppler factor of the cell. The frequency shift (FS) switch selects between using
 860 the local f_{calc} or the global f_{obs} in the emission calculations. The FS facility allows for a
 861 direct user-defined emission dependence on frequency to be introduced ([31] pg. 199:
 862 Simplified synchrotron jet), in the form of a function $S_{\text{obs}} = S_{\text{obs}}(f)$.

863 9.4.3. The DB switch

864 The DB switch offers the option of using the Doppler boosting effect.

865 9.4.4. The speed tweak parameter

866 A test is introduced, whereby matter velocity is multiplied, on a global scale, by
 867 a 'speed tweak' factor. This offers a quick way to observe the impact, on the synthetic
 868 image, of altering the hydrodynamic speed in post-processing, for the same simulation
 869 run. The natural value of tweakspeed is 1. At low tweak speed factors (less than 1) the
 870 effects, on the final image, of both DB and FS, are reduced, and vice versa. The maximum
 871 for tweakspeed is $c/u_{(\max)}$, above which velocities higher than c are artificially created in
 872 the grid.

873 9.5. rlos210

874 rlos version 2.10 includes a unified, functionalized, modular approach. The XZ
 875 and YZ versions were merged for both focused beam and parallel LOSSs. Code was
 876 reorganised, and a series of tests are included.

877 9.6. rlos210 commentary transcript

878 This is the latest version of rlos. Version 2 is a major upgrade of original rlos code.
 879 This time, the programme was broken up into procedures and functions with a modular
 880 structure.

881 The programme allows the user to select which case to simulate, through an external
 882 parameter file. There is a unified approach, where the same modules operate on different
 883 geometries, through parameterization.

884 The user may select the values of the parameters of rlos version 1, and fully employ
 885 them. As mentioned above, there is no more a different version of rlos for XZ and YZ
 886 plane image formation. Now, there is one version of the code for both cases. Furthermore,

887 for each of those cases the user may select either radiograph or camera obscura imaging
888 technique.

889 The radiograph setup has all lines of sight parallel to each other, just like rlos v.1.
890 This means the film (fiducial imaging screen) is the size of the scene (grid), like an X-ray
891 medical image. The latter type of image shows clearly the various details of the system.

892 On the other hand, camera obscura, or focused beam, has a focal point where the
893 eye of the fiducial observer is located. The imaging screen, in camera obscura, is of
894 varied size: It may be equal, or smaller to the grid slice, at a given point along either
895 the x or y axis depending on YZ or XZ imaging plane case. At the moment, the fiducial
896 imaging screen must be parallel to the corresponding side of the grid, i.e. either XZ
897 or YZ. Screen location on-axis may vary within the grid. The smaller the screen is, the
898 smaller the image.

899 The focal point may reside either on the side of the grid or outside the grid but
900 within the limits of the projection of the XZ or YZ plane. It may have a negative or zero
901 axis position, but its two planar coordinates must be smaller than the grid size.

902 Direction angles are no longer necessarily constant throughout the calculation: for
903 the focused-beam case, each LOS is drawn with a different set of azimuth (phi1) and
904 elevation (phi2) angles. Angles are calculated using the lines that connect the focal point
905 and the imaging screen point, which is the target point for the LOS.

906 The LOS then begins from the focal point if it resides on the grid side or from the
907 LOS entry point, calculated suitably. From then on, it advances using aiming algorithms,
908 trying to pass through the targeted screen point. It normally obtains the target or closely
909 misses it. In general, the higher the resolution is, the better the accuracy in this respect.

910 For GR pseudo-Newtonian simulations, a logical next step is to introduce D(phi1),
911 D(phi2), i.e., alter angles along an LOS from cell to cell according to the effect of the
912 potential.

913 Then, innermost jet workings may be imaged, if the hydrocode can employ influence
914 from a black hole.

915 9.6.1. Back in time integration along the LOS

916 In this version, calculations may be performed either ahead in time or backwards
917 in time from a selected time instant (tpicked) backwards. For camera obscura, back in
918 time is generally the correct way to proceed. For radiographs, ahead in time also works
919 fine, assuming a suitable fiducial setup of the jet system vs the observer.

920 tpicked is only employed when back in time switch is activated in the external
921 parameter file. tpicked must be generally towards the end of the preselected range of
922 dump files, or timeshots, to be loaded to RAM. At the moment, it is set equal to tmax,
923 for convenience. A sufficient backwards time range must be provided for the LOS, in
924 order to travel back through time without reaching the beginning of the grid. Otherwise,
925 code cannot finish integration along the LOS. When testing, the facility of altering light
926 speed, clight, may be used to study this effect.

927 Pathfinding algorithms were upgraded for this version. For each combination of
928 XZ or YZ and radiograph or camera obscura, a certain set of such pathfinders were
929 employed.

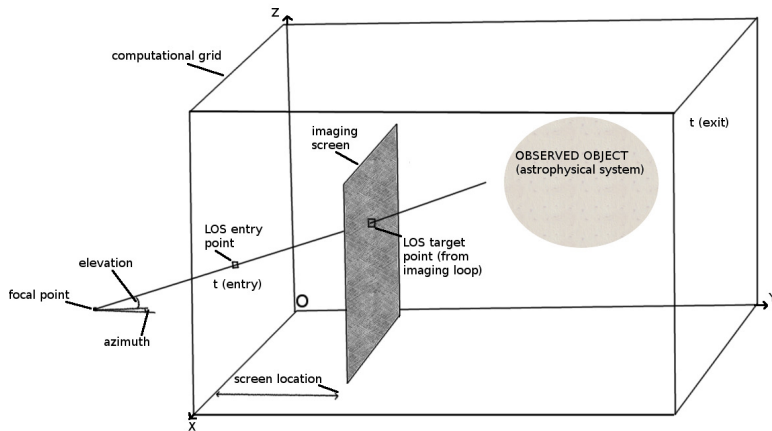


Figure 17. Geometry of focused-beam imaging in rlos, for the case of forward in time calculation. A fiducial screen is where the image is formed.

930 10. Appendix 4: Neutrino emission calculations

931 The presentation in this Section is based on the corresponding Section of [22].

932 10.1. Proton energy loss

933 A number of energy loss mechanisms are included for the hot proton distribution
 934 [19], [6], and [9]. The discussion of this subsection is based on a cell with the following
 935 properties: $(u_x, u_y, u_z, b_x, b_y, b_z, n_p, \phi_1, \phi_2, \alpha) = (-0.3780c, 0.4480c, 0.0124c, 10^5 G, 10^6 G, 10^5$
 936 $G, 2.1 \times 10^{11} \text{ cm}^{-3}, 1.047 \text{ rad}, 5.00 \times 10^{-7} \text{ rad}, 2.0)$, where u stands for velocity and b for
 937 magnetic field along directions x , y , or z . In the following, n is the jet proton density, and
 938 α is the high-energy proton distribution spectral index. As an exception, Figure 22 uses a
 939 velocity vector of $(0.2, 0.8, 0.1)c$. Figures 18, 19, 20, 21, 22 and 23 are taken from [22].

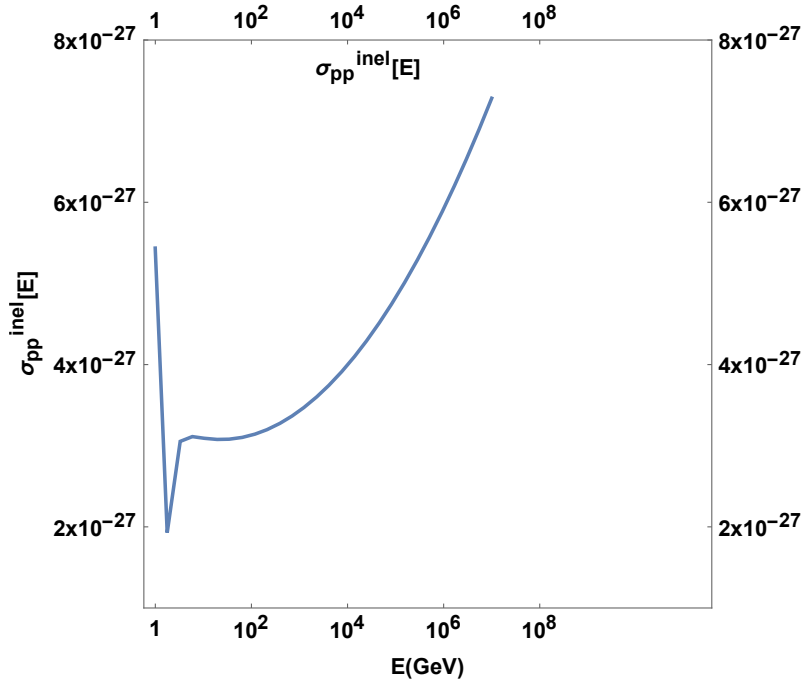


Figure 18. Inelastic proton–proton collision standard plotted with energy. It demonstrates rather small variation (linear vertical scale) of its value over a large energy range (logarithmic horizontal scale), covering and exceeding the energy span required for the calculations that follow later in this paper.

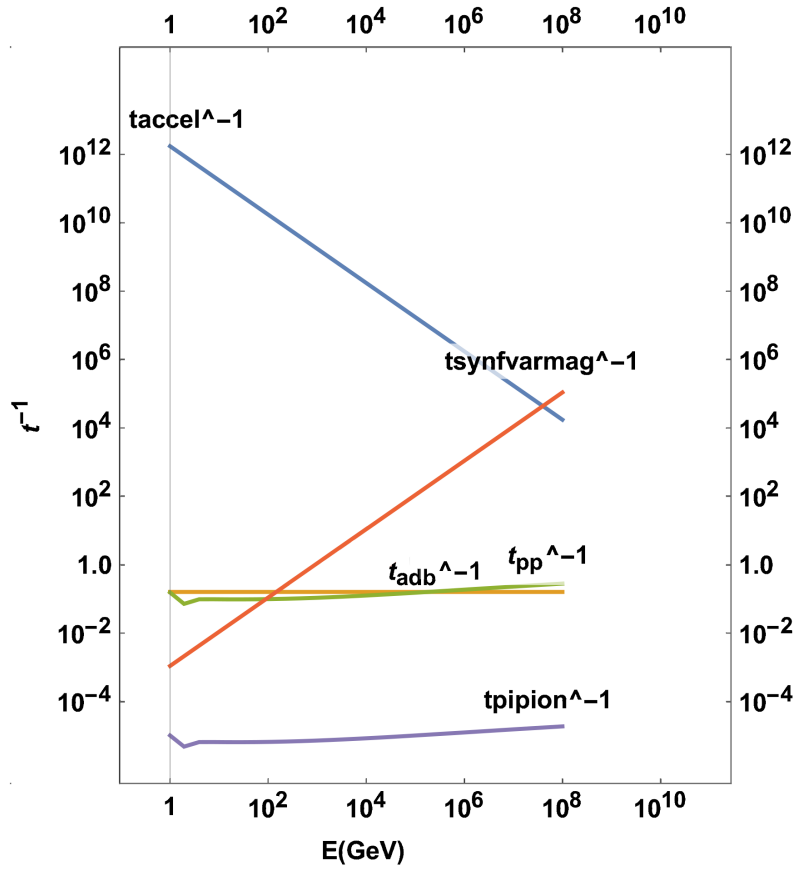


Figure 19. Non-thermal proton distribution energy loss time scales, for various loss mechanisms, drawn with energy in GeV. t_{accel} is the proton acceleration time scale at shocks. $t_{\text{synfvarmag}}$ stands for the synchrotron mechanism loss time scale, using a magnetic field that varies from point to point within the jet. t_{adb} is the adiabatic loss time scale, t_{pp} is the (hot–cold) proton–proton collision timescale. t_{piion} stands for the pion decay timescale t_{π} .

A hot proton upper energy cutoff at $E \leq 10^6$ GeV is used. The adiabatic system expansion time scale is taken to be [6]

$$t_{\text{adb}}^{-1} = \frac{2}{3} \frac{u_{\text{b(adb)}}}{z_j} \quad (36)$$

with $z_j = 10^{11}$ cm being the characteristic width of the jet system at the neutrino emission size scale. For this calculation, $u_{\text{b(adb)}}$ is preset to 0.8, for a 0.8c jet.

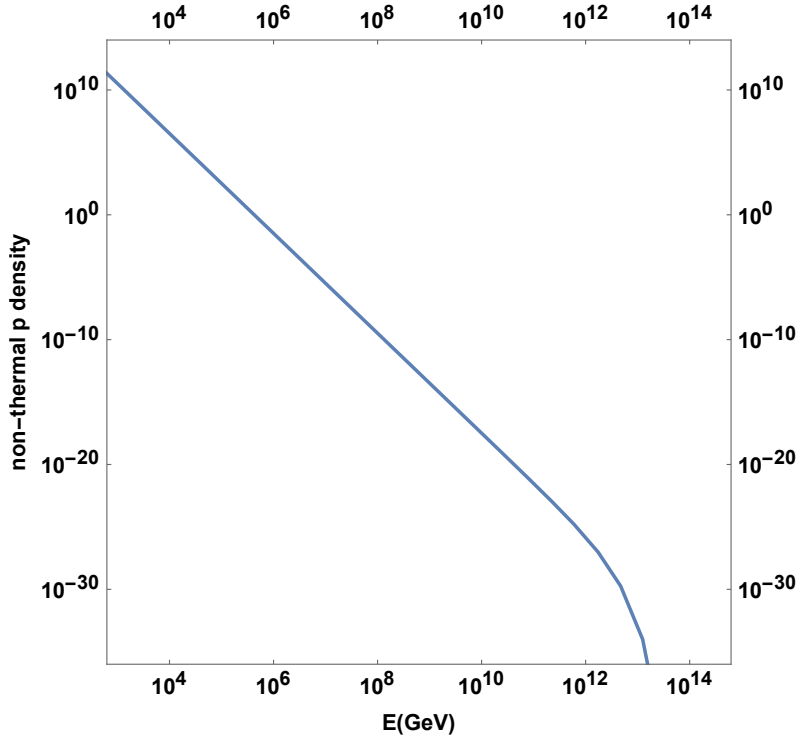


Figure 20. Density of nonthermal protons in the jet using a high-energy cutoff feature plotted with energy.

For the p-p collision energy loss mechanism,

$$t_{pp}^{-1} = n c \sigma_{inel,pp}(E_p) K_{pp} \quad (37)$$

where n is the bulk flow number density, $K_{pp}=0.5$ [6]. Equation 37 is justified if we consider a small cube of matter of number density n , moving at speed (near) c , having a surface A perpendicular to its direction of motion. Then, $n*c$ has the dimensions of $\text{cm}^{-2} \times \text{s}^{-1}$. This is then multiplied by the inelastic p-p collision cross-section [6]

$$\sigma_{pp}^{(inel)} = (34.3 + 1.88L + 0.25L^2) \times [1 - (\frac{E_{th}}{E_p})^4]^2 \times 10^{-27} \text{ cm}^2 \quad (38)$$

⁹⁴² L=ln(E_p/1000GeV), E_{th}=1.2 GeV. In Figure 18, $\sigma_{pp}^{(inel)}$ is plotted.

The pion decay timescale is

$$t_\pi = t_{\pi 0} \Gamma_\pi + t_{esc} \quad (39)$$

where Γ_π is the pion Lorentz factor and

$$t_{\pi 0} = 2.6 \times 10^{-8} \text{ s} \quad (40)$$

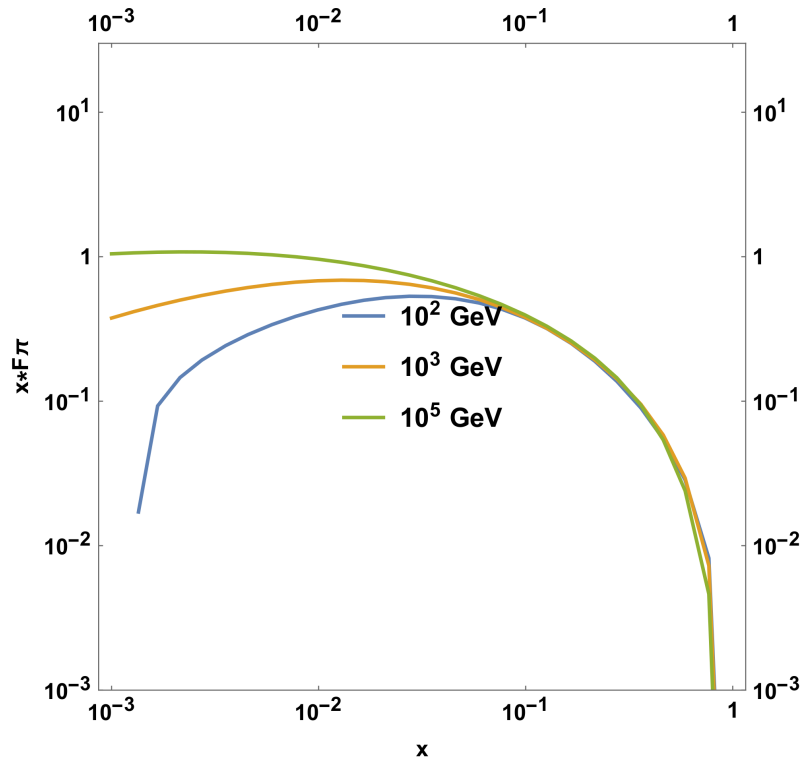


Figure 21. $F_{\pi}^{(pp)}\left(x, \frac{E}{x}\right)$ function, Equation 49, corresponding to the pion spectrum emerging from a single (hot-cold) proton collision, multiplied by $x = \frac{E_{\pi}}{E_p}$. Calculated at three different energies of the hot proton.

In the calculations, we employ the form

$$t_{\pi} = t_{\pi 0} \left(\frac{E_{\pi}}{m_{\pi} c^2} \right) + t_{\text{esc}} \quad (41)$$

where m_{π} is the pion mass. The light escape time t_{esc} is a sensitive parameter of the model.

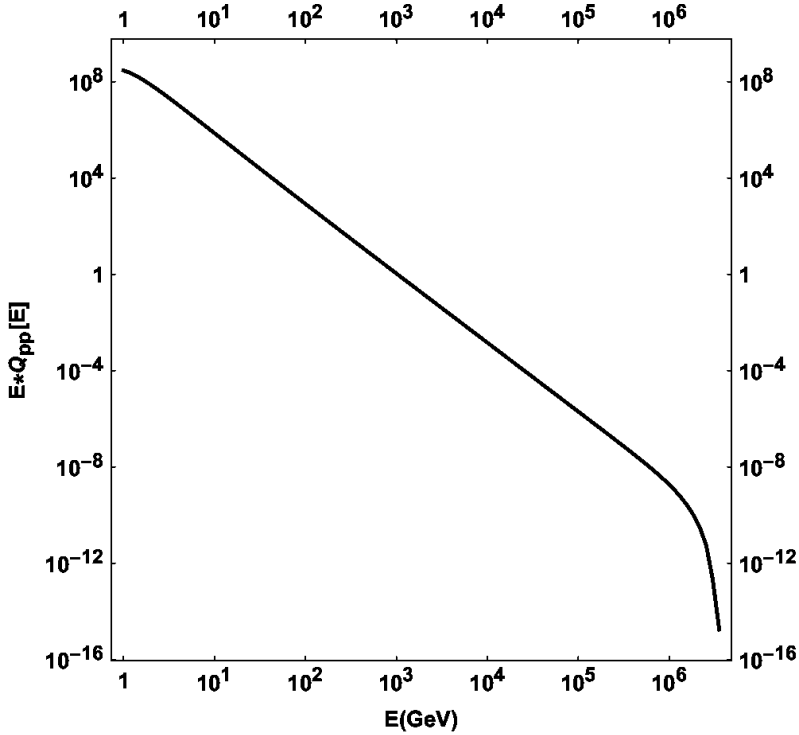


Figure 22. Pion injection function Q , weighted by pion energy, measured in non-normalized units, describing the spectrum emerging from many (non-thermal-thermal) p-p collisions. Contributions rapidly decline as particle energy increases. This figure uses a test velocity vector of $(0.2, 0.8, 0.1)c$.

The synchrotron hot proton energy loss time scale is [6]

$$t_{\text{sync}}^{-1} = \frac{4}{3} \left(\frac{m_e}{m_p} \right)^3 \frac{1}{8\pi c m_e} \sigma_T B^2 \frac{E_p}{m_p c^2} \quad (42)$$

m_e is the electron mass and m_p the proton mass. $\sigma_T = \frac{8\pi}{3} \left(\frac{e^2}{m_e c^2} \right)^2 = 6.65 \times 10^{-25} \text{ cm}^2$ is the Thompson cross-section, and B is the local magnetic field. The proton's Lorentz factor Γ_p is written as $\frac{E_p}{m_p c^2}$, in order to facilitate energy-dependent calculations later on. In summary,

$$t_{\text{loss}}^{-1} = t_{\text{sync}}^{-1} + t_{\text{adb}}^{-1} + t_{\text{pp}}^{-1} \quad (43)$$

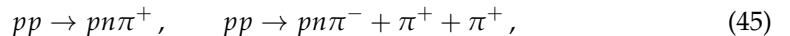
The time-scales of the different energy-loss mechanisms are presented in Figure 19.

946 10.2. Particle cascades in the jets

Hot-cold proton interaction results to a distribution of high-energy pions, which then decay, allowing for the creation of energetic neutrinos. We have [42,63–65]

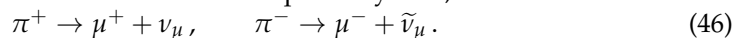


for neutral pions π^0 , and



947 for π^\pm .

Neutral pions π^0 decay to gamma rays. On the other hand, π^\pm mainly decay to an antimuon and a muonic neutrino, or to a muon and an antineutrino (prompt neutrinos) [63],[65]. We therefore obtain neutrinos that escape the system, after the cascade.



948 As an approximation, we do not consider neutrino production through secondary
949 channels or delayed neutrinos.

For each successive particle population in the above cascades, the transport equation for nonstochastic phenomena and for time-independent transport (transport time much less than the time step of the dynamic simulation), takes a simplified form:

$$\frac{\partial N}{\partial E} + \frac{N}{t_{\text{loss}}} = Q(E, \vec{r}) \quad (47)$$

where \vec{r} is the spatial position vector, N is the particle density of the daughter population, and Q is its injection function.

A power-law distribution is assumed for protons (Figure 20 shows power-law fast proton density), replacing the solution of the first transport equation in the cascade. Afterwards, along the cascade, we calculate the properties of resulting particle distributions [19].

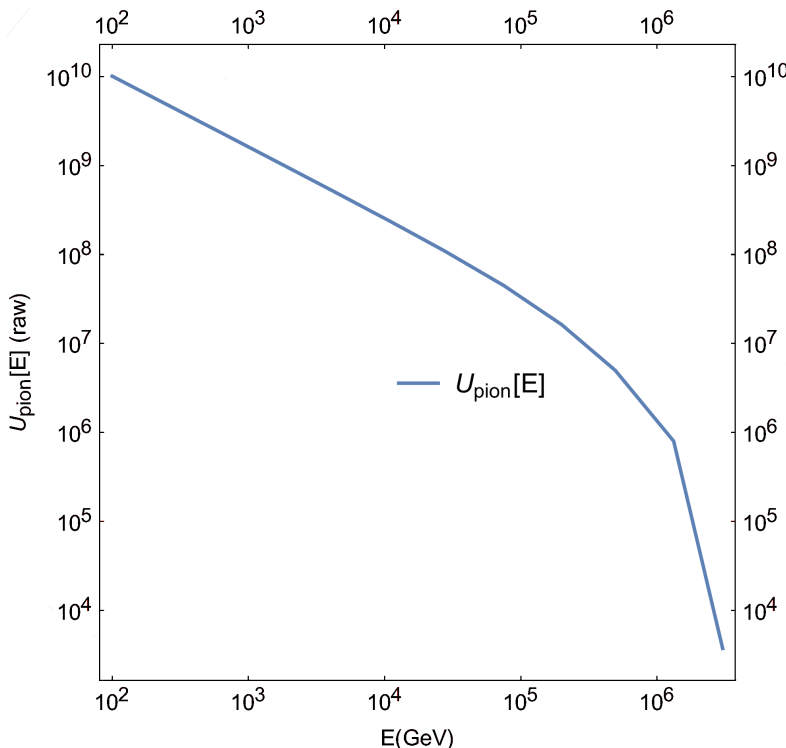


Figure 23. Pion energy distribution plotted in non-normalized units versus energy. In the software, the above distribution is represented by function U .

10.3. Lorentz transform of high E proton distribution

For the calculation of the fast proton distribution, the relevant directional equation (direction is defined by the angle θ between velocity and line of sight) can be found in [37] [66]. The selected variant originates from [37], minus a geometry factor that is here absorbed into the normalization factor [22]

$$n(E, \theta) = \frac{\Gamma^{-\alpha-1} E^{-\alpha} (1 - \beta \cos(\theta) \sqrt{1 - \frac{m^2 c^4}{E^2}})^{-\alpha-1}}{[\sin^2(\theta) + \Gamma^2 (\cos(\theta) - \frac{\beta}{\sqrt{1 - \frac{m^2 c^4}{E^2}}})^2]^{\frac{1}{2}}} \quad (48)$$

where Γ is the Lorentz factor of the particles in a tiny volume.

10.4. Pion injection function and pion energy distribution

For each fast–slow proton interaction, a spectrum of possible pion energies exists, given by function F_π [19], [6] [9].

$$F_\pi^{(pp)}\left(x, \frac{E}{x}\right) = 4\alpha B_\pi x^{\alpha-1} \left(\frac{1-x^\alpha}{1+rx^\alpha(1-x^\alpha)}\right)^4 \left(\frac{1}{1-x^\alpha} + \frac{r(1-2x^\alpha)}{1+rx^\alpha(1-x^\alpha)}\right) \left(1 - \frac{m_\pi c^2}{xE_p}\right)^{\frac{1}{2}} \quad (49)$$

where $x = E/E_p$, $B_\pi = \alpha' + 0.25$, $\alpha' = 3.67 + 0.83L + 0.075L^2$, $r = 2.6/\sqrt{\alpha'}$, $\alpha = 0.98/\sqrt{\alpha'}$ [6,19].

Figure 21 xF_π is plotted with the fraction x for different fast proton energies.

Pion injection function $Q_\pi^{(pp)}$ comprises pion contributions at each pion energy to that pion energy from spectrum F of all potential p-p interactions.

$$Q_\pi^{(pp)}(E, z) = n(z)c \int_{\frac{E}{E_p^{(\max)}}}^1 \frac{dx}{x} \left(\frac{E}{x}, z\right) F_\pi^{(pp)}\left(x, \frac{E}{x}\right) \sigma_{pp}^{(inel)}\left(\frac{E}{x}\right), \quad (50)$$

x is the fraction of the pion energy to proton energy, and $n(z)$ is the jet flow proton density.

Figure 22 plots $Q_\pi^{(pp)}$ versus pion energy E_π .

In order to obtain the pion distribution, the following transport equation is employed:

$$\frac{\partial N_\pi}{\partial E} + \frac{N_\pi}{t_{loss}} = Q_\pi^{(pp)}(E, z) \quad (51)$$

where $N_\pi(E, z)$ denotes the pion energy distribution. Then

$$N_\pi(E) = \frac{1}{|b_\pi(E)|} \int_E^{E^{(\max)}} dE' Q_\pi^{(pp)}(E') \exp[-\tau_\pi(E, E')], \quad (52)$$

and

$$\tau_\pi(E', E) = \int_{E'}^E \frac{dE'' t_\pi^{-1}(E)}{|b_\pi(E'')|}. \quad (53)$$

$b_{\pi(E)} = -E(t_{sync}^{-1} + t_{adb}^{-1} + t_{\pi p}^{-1} + t_{\pi\gamma}^{-1})$ is the energy loss rate of the pion. As an approximation, the last term in the latter expression is omitted. In Figure 23 plots nemiss [49] software function U ($U_{analytical}$), representing N_π , with pion energy.

The above calculations are performed for each computational cell. A cell is macroscopically large inasmuch as only the deterministic portion of the transport equation is employed, in turn rendering it deterministic. Again, we take the characteristic scale (mean free path) of the radiative interactions to be smaller than the cell size, leading to the containment of particle interactions within a given hydrocode cell. Furthermore, the time scale for the radiative interactions is taken to be smaller enough than the hydrocode's time step, so that a cell's radiative interactions belong to a single time step each time.

10.5. Neutrino emissivity

As mentioned in the main text, the emissivity of prompt neutrinos [5,6,19,20], is

$$Q_{\pi \rightarrow \nu}(E) = \int_E^{E_{\max}} dE_\pi t_\pi^{-1}(E_\pi) N_\pi(E_\pi) \frac{\Theta(1 - r_\pi - x)}{E_\pi(1 - r_\pi)}, \quad (54)$$

E is neutrino energy, $x = E/E_\pi$, $r_\pi = (m_\mu/m_\pi)^2$ and t_π is the pion decay timescale. $\Theta(\chi)$ is the theta function [6,42]. Neutrino emissivity is calculated for each individual cell using the angle of the local velocity to the LOS crossing that cell.

